Convection initiation and bore formation following the collision of mesoscale boundaries over a developing stable boundary layer: a case study from PECAN

Guo Lin[1,2], Coltin Grasmick[3], Bart Geerts[3], Zhien Wang[1,2*], and Min Deng[2,3]

[1]*Department of Atmospheric and Oceanic Sciences, University of Colorado, Boulder, Colorado*

[2] *Laboratory for Atmospheric and Space Physics, University of Colorado, Boulder, Colorado*

[3] *Department of Atmospheric Science, University of Wyoming, Laramie, WY*

Revised submission to *Mon. Wea. Rev.*

4 Jan 2021

**Corresponding author*: Zhien Wang, Laboratory for Atmospheric and Space Physics and Department of Atmospheric and Oceanic Sciences, University of Colorado Boulder, 3665 Discovery Dr., Boulder, CO 80303. Email: Zhien.Wang@colorado.edu

Abstract

This observational study documents the consequences of a collision between two converging shallow atmospheric boundaries over the central Great Plains on the evening of 7 June 2015, at a time when a stable boundary layer (SBL) started to form. This study uses data from a profiling airborne Raman lidar (the Compact Raman Lidar, or CRL) and other airborne and ground-based data collected during the Plains Elevated Convection At Night (PECAN) field campaign to investigate the collision between a weak cold front and the outflow from a MCS. The collision between these boundaries led to the lofting of high CAPE/low CIN pre-frontal air, resulting in deep but short-lived convection, as well as an undular bore. Because the airmass behind the outflow boundary was deeper and denser than the post-frontal airmass, the bore propagated over the latter. This bore, tracked by the CRL for about three hours as it traveled north over the shallow cold-frontal surface, evolved into a soliton. This case study is unique in describing the detailed vertical structure of thermodynamics and convective potential of interacting boundaries and a resulting bore with temporally and spatially resolved CRL boundary layer measurements.

1. Introduction

Convergent boundaries may deepen boundary layer (BL) humidity to create conditions favorable for initiating deep convection in areas where deep convection otherwise is inhibited (Wilson and Schreiber 1986; Geerts et al. 2017). Over land in the warm season, these boundaries are visible in low-elevation radar reflectivity scans as 'fine lines' because of small, weakly-flying insects lofted into the BL (Russell and Wilson 1997; Geerts and Miao 2005). Since Purdom (1982) noted the potential for using these radar fine lines for identifying possible locations for convection initiation (CI), forecasters have been monitoring these fine lines on the lookout for impactful weather. In addition to enhanced scattering, a wind shift is usually present across the boundary, which provides another method for boundary detection via Doppler radar (Wilson and Schreiber 1986) or lidar (Intrieri et al. 1990).

In the daytime convective BL, over flat terrain, these boundaries are solenoidally forced, i.e., driven by a density difference (Miao and Geerts 2007), e.g., a thunderstorm outflow boundary (Wakimoto 1982) or a synoptic front (Geerts et al. 2006). When the land surface starts to cool in the evening, and a stable boundary layer (SBL) forms, these density currents may transition to bores and solitary waves (e.g., Clarke 1972). A bore is a gravity wave response generated when a density current intrudes into a stable layer (Crook 1988; Rottman and Simpson 1989; Haghi et al. 2019). The importance of low-level shear on the behavior of undular bores is less understood (Haghi et al. 2019). One of the key objectives of the 2015 Plains Elevated Convection at Night (PECAN) field campaign regards the role of bores in CI and the maintenance of MCSs across the Great Plains (Geerts et al. 2017).

The dynamics of CI along a convergent boundary are generally well understood (e.g., Harrison et al. 2009). CI occurs when a sufficiently large air parcel is lifted above its Level of

61 Free Convection (LFC). In the presence of a SBL and forced vertical motion, profiles of parcel
62 LFC and CAPE can be examined to estimate whether a parcel emerging from any layer can
63 realize elevated CAPE (e.g., Grasmick et al. 2018). In a well-mixed BL, ambient wind shear
64 matters as well; in the widely accepted RKW theory (Rotunno et al. 1988), new convective cells
65 are more likely to form (and MCSs are more likely maintained) if the solenoidally-driven
66 horizontal vorticity of a boundary matches the vorticity of the ambient vertical wind shear in
67 magnitude, but is opposite in sign.

68 CI is often difficult along a single propagating boundary. Collisions between boundaries
69 propagating in different directions and/or at different speeds increase the likelihood for CI
70 because they lead to transient deeper lifting (Kingsmill 1995). Different boundary collisions have
71 been described, for example, between two thunderstorm outflows (Karan and Knupp 2009),
72 between a sea-breeze front and an outflow boundary (Kingsmill 1995), and between a dryline
73 and a cold front (e.g., Wakimoto et al. 2006). CI along boundary collisions is difficult to predict:
74 the precise geometry of the boundaries (e.g. depth and orientation) determining upward
75 displacement is usually unknown and any resulting CI is often displaced horizontally
76 (Weckwerth and Parsons 2006).

77 Density current collisions frequently generate atmospheric bores (Kingsmill and Crook
78 2003; Karan and Knupp 2009). Simpson (1987) conceptualized bore generation in density
79 current collisions based on laboratory experiments. Kingsmill and Crook (2003) applied this
80 model to cases of colliding gust fronts and sea-breeze fronts. Theoretically, if two colliding
81 density currents are similar in depth and density, the structural evolution is symmetrical: the
82 region of colliding density current mass bulges upwards and this bulge subsequently evolves into
83 two bores, propagating away from the collision line in opposite directions. However, most

84 colliding currents are not identical, so collisions commonly result in the less dense current
85 overriding the denser current (Fig. 1 in Kingsmill and Crook 2003).
86 This paper documents the collision between thunderstorm outflow (i.e., "gust front") and
87 a cold front, which results in both CI and a bore. As will be shown below, the gust front is denser
88 and shallower than the encroaching cold-frontal airmass, producing a highly non-symmetrical
89 evolution (see Fig. 1). The primary objective of this study is to document the evolution of two
90 colliding density currents, the resulting CI, and bore, by means of high-resolution vertical
91 transects of humidity and temperature obtained from an airborne Raman lidar. The current,
92 sparsely spaced 12-hourly sounding network offers low horizontal and temporal profiles. Surface
93 stations are also sparse. Geostationary satellites have high temporal resolution but do not provide
94 adequate vertical resolution in the BL. As a result, a small-scale, rapidly evolving convective
95 plume from a convergent boundary is difficult to monitor using the current operational network.
96 The rare airborne measurements presented here have sufficient resolution to describe a density
97 current collision.
98 Our analysis uses data derived from the airborne Raman lidar such as CAPE and CIN,
99 together with an array of ground-based measurements, to reveal the vertical structure of the
100 collision process and explain observed CI. Such novel thermodynamic analysis is a powerful tool
101 to assess convective potential and improve CI forecast (Weckwerth and Parsons 2006).
102 Several observational studies have documented eastward and southward propagating
103 bores that formed when MCS outflow intruded into the SBL in the Great Plains (Grasmick et al.
104 2018; Haghi et al. 2019; Johnson and Wang 2019; Loveless et al. 2019; Parsons et al. 2019).
105 This study documents a bore propagating in an uncommon direction, towards the north. It
106 formed after the outflow intruded into a cold front, rather than the SBL. The Raman lidar and

ground-based network provides a thermodynamic perspective of the environment before, during, and after the collision and bore formation.

Section 2 describes the datasets and instruments for this case study. An overview of the MCS and Raman lidar transects are presented in section 3. The vertical structure of the converged boundaries is detailed in section 4. The bore, formed upon boundary collision, and whether the environment supports bore formation and propagation are analyzed in section 5. The findings and conclusions are discussed in section 6.

2. Data and Methodology

2.1 The 2015 PECAN campaign

The 2015 PECAN field campaign aimed to understand the driving mechanisms of nocturnal MCSs, bores, and CI in the presence of a SBL and a low-level jet (Geerts et al. 2017). Cold-pool-generated bores and related solitary waves were found to be relatively common during PECAN. Among other objectives, the PECAN campaign aimed to advance the understanding of the generation and evolution of bores, and their role in CI. This study contributes to that objective.

2.2 PECAN airborne data

Three aircraft were deployed in PECAN, but the University of Wyoming King Air (UWKA) was the only aircraft to focus on the lower-tropospheric environment during PECAN, where CI and bores/solitary waves originate. The UWKA carried an array of in situ probes and a high-resolution Compact Raman Lidar (CRL; ~300 m horizontal and ~100 m vertical resolution) (Wu et al. 2016). The CRL can provide accurate retrievals of water vapor mixing ratio (WVMR),

130 lidar scattering ratio (LSR), and temperature in the lower troposphere (Liu et al. 2014; Wu et al.
131 2016). The CRL provides WVMR with a mean difference of 0.2 g kg^{-1} compared to in situ
132 measurement (Wang 2020). Due to the photomultiplier tube ring-noise in CRL's temperature
133 measurements before 15 June during PECAN (Wang et al. 2016), CRL temperature
134 measurements only can be used to provide horizontal temperature variations; the temperature
135 cross-section is calculated by adding the CRL derived temperature variation cross-section to a
136 mean low-level temperature profile from proximity radiosonde data. The random errors of CRL
137 temperature measurements increase with ranges, and the near-surface random errors could up to
138 1.5 K (Wu et al. 2016). Aircraft turning also introduces surface signal contaminations in
139 temperature retrievals near the surface. Thus, the lowest 200 m temperature layer is removed.
140 The flight-level in situ WVMR and virtual potential temperature on the top of CRL profiles add
141 to cross-sections and serve as CRL validation.
142 The LSR is a normalized parameter of total backscattering to molecular backscattering.
143 The minimum value (1.0) represents scattering by air molecular only, and larger values (> 1.0)
144 represent additional aerosol backscattering. The CRL, which was pointed nadir, was
145 complemented by the zenith-pointing Wyoming Cloud Lidar (WCL, Wang et al. 2009), to
146 provide lower-tropospheric LSR profiles. The synergy of flight-level measurement (1 and 10 Hz)
147 with a full lower-tropospheric LSR profile (above and below flight level) is uniquely powerful
148 for studying the dynamic and thermodynamic environment across the converged boundary and
149 multiple fine lines. In this study, we use mean sea level (MSL) to reference height because of
150 varying ground elevation along flight legs (although small) and the ease with which airborne,
151 surface, and profile observations can be compared.

This study derives CAPE, CIN, and the distance to each parcel's level of free convection (LFC), following Grasmick et al. (2018) and Lin et al. (2019). In essence, CRL temperature and moisture at each time step (interval of 3s) at any height between the ground and flight level are combined with proximity radiosonde data above flight level (in this case, the 0306 UTC radiosonde released from MP1) to reconstruct a sounding for each UWKA profile. Then, each thermodynamic profile is used to calculate the profiles of lifting condensation level (LCL), LFC, CAPE, and CIN.

2.3 Ground-based data in PECAN

During PECAN, a series of surface mesonet vehicles were deployed, equipped with roof-mounted instruments to measure temperature, pressure, humidity, and winds at 1 Hz (Roberts et al. 2008). Data from one of these vehicles, called the "mobile mesonet 1" (MM1), is used to characterize the surface characteristics of the different airmasses as it crossed the convergent boundary (Wagner and Ziegler 2017).

PECAN Integrated Sounding Arrays (PISAs) with four mobile PISA units (MP) and six fixed units (FP) were deployed during intensive observation periods (IOPs). The FPs were continuously operating. MPs were entirely contained within a vehicle and can be deployed to different locations but remained stationary for individual IOPs. Specifically, surface-based and radiosonde data from MP1 and radiosonde data from FP2 are used in this study (Klein et al. 2016; Turner 2016; Vermeesch 2015). MP1 is equipped with instruments to measure surface-based temperature, pressure, humidity, and wind at 1 Hz. Two MP1 radiosondes, spaced three hours apart, supplement the temperature and mixing ratio retrieved below the UWKA flight level. The radiosonde data were concatenated to the top of the low-level CRL data and used to

175 construct profiles of temperature and mixing ratio from the surface to 350 mb for each CRL
176 profile. By allowing the low-levels to vary along the flight path, stability parameters such as
177 elevated CAPE and CIN can also vary along the flight path as discussed previously.
178 Finally, Atmospheric Emitted Radiance Interferometer (AERI) data from MP1 were used
179 in this study (Turner 2018). An AERI is a ground-based remote sensor measuring spectrally
180 resolved downwelling infrared radiation to retrieve vertical profiles of water vapor and
181 temperature, using an optimal estimation-based physical retrieval algorithm (Knuteson et al.
182 2004a, b). In clear-sky situations (or cloud bases above 2 km), the mean bias errors with respect
183 to radiosonde profiles are less than 0.2 K and 0.3 g kg^{-1} for temperature and water vapor mixing
184 ratio, respectively, but its random errors could be significantly higher than the mean biases
185 (Turner and Lohnert 2014).
186
187 *2.4 Operational data*
188 This study employs the operational network of radar and surface observations. The radar
189 reflectivity factor and mean radial velocity from the Next Generation Weather Radar (NEXRAD)
190 system (Crum et al. 1993) are used to show storm wind structure and to place the UWKA flight
191 track in the context of the MCS, cold front, outflow boundaries, and bores.
192 The Meteorological Assimilation Data Ingest System (MADIS) is a fine-scale grid of
193 interpolated surface meteorological observations, used to initialize and evaluate weather and
194 climate models, provided by the National Oceanic and Atmospheric Administration (NOAA).
195 MADIS combines NOAA data sources with non-NOAA data into a common format with
196 multiple quality control procedures (details at https://madis.ncep.noaa.gov/madis_qc.shtml) and

provides a finer resolution depiction of environmental conditions than synoptic-scale data (Miller et al. 2005).

3. Overview of the mesoscale environment and air mass characteristics

Early on 8 June (02:00 UTC; 21:00 central daylight time on 7 June, 3 minutes after local sunset), a southwest-northeast-oriented MCS extended from the central Texas panhandle to northern Oklahoma. The primary mission of this PECAN IOP 6 was to document CI, predicted to develop northeast of the MCS where there was a cold front (marked on the surface analysis map of the Weather Prediction Center at 03:00 UTC; Fig. 2a). This cold front is apparent in the MADIS data (Fig. 2f) at the boundary between northerly and southerly flow in south-central Kansas. The UWKA flight track is shown within the area of interest (small red box in Fig. 2b), where it sampled the cold front, MCS outflow, and post-collision boundary. Tongue-like shapes of temperature and dewpoint contours in the area sampled by the UWKA indicate small-sale thermodynamic features that are hard to identify using MADIS alone due to the relatively coarse resolution and irregular spacing of the data (Fig. 2c and d). The MCS was located on the south side of the cold front, just south of the red box in Fig. 2b. Its downdraft and spreading cold pool are observable where diffluent flow moves outward from the MCS center and the cooler station temperatures (Fig. 2c and d). The MCS outflow boundary is evident in the MADIS surface data as the northward extent of this cold pool.

During the IOP, the KICT Doppler radar observed the southward progression of the cold front and northward progression of the MCS outflow by their respective fine lines (Fig. 3 a, b, c, and d). Weak westerly flow is observed between the two boundaries (light blue between the red dashed line and orange dashed line); its speed is slower than the flow behind the outflow

boundary (darker blue; Fig. 3f and g). The stronger northwesterly flow behind the cold front is also observed in MADIS data (Fig. 2e and f) and marks as a cold front by the Weather Prediction Center (Fig. 2a). The speed of the surface cold front was ~8.0 m s^{-1} at time it passed the MP1 site (estimated from radar loops in the PECAN Catalog Map: http://catalog.eol.ucar.edu/maps/pecan). Behind the cold front, the wind speed was greater than 10 m s^{-1} below 1.25 km MSL height in the same direction as the cold front's motion (Fig. 4a). Since the wind speed behind the boundary is larger than the cold front's propagation speed, there is mass transport, as is common for cold fronts propagating as density currents. Observations by MP1 show the environmental conditions before and after the frontal passage (Fig 5c). The air immediately behind the cold front was only slightly cooler than the prefrontal air, likely a result of its passage at night while temperatures were decreasing. After passage, the temperature continued to decrease with time while the air density and pressure increased (Fig 5b). The water vapor mixing ratio was the most prominent discriminator of these air masses; frontal passage at MP1 was most notable by an increase in WVMR, from ~10 g kg^{-1} to ~15 g kg^{-1} (Fig. 5a). Nevertheless, the decrease in temperature upon frontal passage was benign (Fig. 5a). Even so, convergence and forced-ascent along the cold front triggered local deep convection in the NE corner of Fig 3. The surface outflow speed was 5.6 m s^{-1} when it passed the FP2 site, 55 km away on the southwest of MP1, around 0200 UTC (the FP2 site location shown in Fig. 3), while the wind speed behind the outflow was up to ~7.0 m s^{-1} at 0306 (Fig. 4b). The MCS outflow is a density current with mass transport as the wind speed behind the outflow is larger than outflow's propagation speed.

4. CI and convective potential

The UWKA flew inbound and outbound legs (relative to the MCS) over the region of CI, profiling the thermodynamic structure before and during the initiation of isolated, transient deep convection resulting from the collision of the cold front and outflow boundary. The remote and in situ measurements from the UWKA provided information about the vertical structure of the colliding boundaries and the depth of lifting (Fig. 6). The color-code flight-level tracks by WVMR and virtual potential temperature on the top of CRL profiles are from in situ sensors (Fig.6 a and c) and indicate that CRL measurements reliably capture the spatial variations. As the UWKA flew southeast toward the MCS (the red line in the bottom of Fig. 6c), profiling observations (i.e., transects of WVMR, LSR, and virtual potential temperature in Fig. 6a, b, and c) show warmer, moister air moving southward behind the cold front approaching the MCS. At the same time, the cooler, drier outflow from the parent MCS flowed northward. The well-mixed cold-frontal air with 15 g kg^{-1} of WVMR below 1.5 km MSL (Fig. 6a) was simultaneously sampled by MP1 on the ground (Fig. 5a). The MP1 radiosonde profile at 03:06 UTC also shows a well-mixed layer from the ground to the height of 1.25 km and ~15 g kg^{-1} of WVMR behind the cold front. At the time of the transect in Fig. 6 (02:18 UTC), the cold front and MCS outflow had just collided. Lidar measurements show the moist cold-frontal air mass abutted with the much drier, shallower outflow between 02:10 and 02:21 UTC (Fig. 6a and c). The LSR and WVMR transects show that these correspond to a plume of the cold-frontal, moist air extending up to flight-level (Fig. 6a and b). While crossing this in-progress collision, the upward-looking lidar captured a non-precipitating middle-level cloud base around a height of 3.0 km MSL (Fig. 6b), with a peak flight-level vertical velocity of 3.0 m s^{-1} below cloud base (Fig. 6d). At flight level (2.5 km MSL), as the aircraft briefly sampled the cold-frontal airmass across the collision boundary, the wind shifted from west-southwest to northwest indicating a convergent flow (Fig.

6d) where the relative humidity increased and the temperature decreased (Fig. 6e). The top of the cold front lifted from its original height of ~1.4 km MSL to its LCL at 3.0 km, a ~ 1.6 km vertical displacement (Fig. 6b), i.e., the height of the cloud base observed by the WCL.

In the low levels of the converged boundary (near 02:18 UTC in Fig. 6a), the WVMR transect shows a large water vapor gradient across the transition from the cold-frontal air mass to the MCS outflow, where the WVMR at 1.0 km MSL decreased from 15 to 7 g kg^{-1} over 5 km. This large WVMR gradient shows the different thermodynamic properties of the cold front and outflow. When the surface mesonet designated MM1 moved across this convergent boundary, the WVMR shapely decreased from 15 to 10 g kg^{-1}, the temperature non-linearly dropped from 27 to 21 ^{o}C indicating large fine-scale variability, the air density and sea level pressure (SLP) increased, and wind shifted from NE to SW (Fig. 7). These surface-based measurements are consistent with large near surface water vapor and temperature variations observed by the CRL (Fig. 6).

The transect of virtual potential temperature shows the MCS outflow as a very shallow surface-based cold pool (green and blue color in Fig. 6c around 02:20 UTC). On the outflow side of the collision, the pre-existing environmental air between the cold front and outflow, now lofted above the MCS outflow, contained more water vapor than the MCS outflow below. Even more notable, is the plume of high WVMR (about 11 g kg^{-1}) that could be traced back to the cold-frontal air mass. The horizontal scale of this moist plume is about 5 km, which may be wide enough for deep convection in a high-CAPE weakly sheared environment such as observed by Peters at al. (2019). Clearly, an elevated moist plume of this size cannot be captured by the operational network. If it is sampled by chance by an operational radiosonde, it would be assigned a much larger footprint, and thus err data assimilation and forecasts.

289 The two sides of the converged boundary are also differentiable by aerosol content in the
290 LSR transect. The post-frontal air has a large LSR values (>1.15) up to 1.5 km MSL while the
291 MCS outflow appears nearly devoid of aerosols around the height of 1.0 km (LSR values are
292 close to one), likely due to moist scavenging within/under the MCS, or entrainment of air from
293 above the BL.
294 The MCS cold pool properties remained fairly homogeneous as the UWKA paralleled the
295 storm toward the northeast (Fig. 6f and the blue solid line blow Fig. 6c). Next, the UWKA made
296 two more transects across the collision point (green and orange solid lines blow Fig. 6c),
297 revealing spatial and temporal changes. During the third transect, the CRL shows the
298 development of a new cloud, the top of which is just below flight level, where the CRL signal
299 becomes attenuated near 2.4 km MSL (Fig. 6a, b, and c, 02:26 UTC; within the "green" flight leg
300 delineated below Fig. 6c). This cloud is convective, with flight-level updrafts up to 7 m s^{-1} (Fig
301 6d).
302 During the final transect in this region (orange solid line blow Fig. 6c), the UWKA had
303 descended to a lower flight level and passed through this convective cloud (Fig. 6b, around 02:30
304 UTC); the in situ instruments at flight level detected liquid water (up to 0.08 g m^{-3} in Fig 6d),
305 strong updrafts and enhanced aerosol concentration and humidity just outside cloud (Fig. 6a and
306 b). A brief, intense (~10 m s^{-1}) downdraft was detected on the south side of this cloud, just
307 behind the MCS outflow boundary pushing cooler, drier air north. Just after this fourth transect,
308 the KICT radar observed two cells with heavy precipitation (reflectivity values exceeding 50
309 dBZ) near the updraft measured by the UWKA (Fig. 3c and d), and in-cloud lightning was
310 observed (not shown), which forced the UWKA to leave the area.

311 Initially, the intermediate southwesterly winds (Fig. 3 e, f, and g) were not conducive to
312 deep, vertical updrafts along either boundary in the region of the UWKA transects. The wind
313 direction was away from the MCS outflow (i.e., in the same direction) and nearly paralleled with
314 the cold front. (However, the cold front changed orientation northeast of KICT, which is also
315 where additional CI was observed). Where the two boundaries collided, the flow was highly
316 convergent. The meeting of solenoidal vorticity cores of opposite sign (one from each boundary)
317 led to a strong but transient updraft. By 0205 UTC (Fig. 3a and e), the cold front and MCS
318 outflow had already collided west of the UWKA's position, but this was not immediate followed
319 by CI. This may be due to weaker outflow (light green) further away from the parent MCS.
320 Another possibility could be the orientation of the two fine lines, which allow intermediate air to
321 escape to the east without being forced vertically (Wilson and Schrieber 1986; Frank and Kucera
322 2003). This westerly acceleration ahead of the collision point (which moved eastward like a
323 zipper; Fig. 3 a, b, c and d) enhanced convergence, eventually leading to the CI observed by the
324 UWKA and CRL. Doppler velocity at KICT does show an increased westerly wind between the
325 two boundaries, which also resolved as an increasing westerly wind by the MADIS data (Fig.
326 2e). However, clean air (devoid of scatters) before the collision makes the radar analysis
327 inconclusive.
328 The convection triggered by the convergent boundary was short-lived, decaying rapidly
329 as it moved eastward (Fig. 3c-d). We now investigate the convective potential of the air parcels
330 on both sides of the convergent boundary by deriving CAPE, CIN, distance to LCL, and distance
331 to the LFC using the CRL temperature and moisture fields and the method discussed in Section
332 2.3.

The derived CRL's CAPE, CIN, and displacement transects (Fig. 8) reveal the parcels on different sides have different instability. The relatively warm and moist cold frontal airmass has large values of CAPE (with pockets > 1,300 J kg^{-1}) and CIN (< 300 J kg^{-1}). As expected, the outflow was more statically stable containing low CAPE (generally < 200 J kg^{-1}) and large CIN (generally > 400 J kg^{-1}) below 1.25 km. In general, the drier air within the outflow (Fig. 8d and e) needed more uplift to reach its LCL (~2 km) and LFC (~4 km or no LFC) than the cold-frontal air (LCL <1.5 km, and LFC 1.5-2.5 km uplift). Both air masses were colder and more stable than the prefrontal BL air, which logically is the most likely source of the observed deep convection. The convergence that results from these two air masses colliding lifts parcels about 1.6 km as seen in the WVMR and LSR plumes (02:18 UTC in Fig. 6). This lifting is sufficient for air within this plume to overcome environmental CIN, reach its LFC and LCL, resulting in deep convection, as observed.

5. Bore and solitary waves

5.1 Bore formation

In addition to the CI, the cold front-gust front collision also produced a bore-like wave structure with multiple radar fine lines traveling northward on the top of the cold-frontal air mass, in the opposite direction of the cold front. As they passed by MP1 around 03:45 UTC (Fig. 5), surface observations showed periodic wind speed and direction changes that are more similar to gravity waves rather than a single density current gust front. The bore gravity waves could be seen propagating toward the NNW as multiple, parallel fine lines in the base reflectivity and Doppler velocity of the KDDC radar (Fig. 9). After the transects that documented the boundary collision and CI, the UWKA executed two sets of racetrack flight patterns that were nearly

perpendicular to these bore waves: the first racetrack consisted of four legs (Fig. 9a and b), and the second, further west, had six (Fig 9c and d).

Nocturnal bores are common during the summer months in the Great Plains and most frequently occur when MCS outflow boundaries intrude into a SBL (Geerts et al. 2017; Haghi et al. 2017, 2019; Mueller et al. 2017). The few case studies that have documented bore development from colliding boundaries, i.e. Wakimoto and Kingsmill (1995), Kingsmill (1995), Kingsmill and Crook (2003) and Karan and Knupp (2009), all relied on continuous radar and surface station or tower measurements, and they all emphasized bore kinematics, obtained from Doppler radar. For instance, Karan and Knupp (2009) display cross-sections of winds during the collision of two gust-fronts using a WSR-88D Doppler radar, supplemented with measurements from a 915-MHz wind profiler. Their wind analysis reveals two separate updrafts that combined to form a wider, more intense, short-lived updraft. In their case, isolated CI appeared during the collision 30-40 km away from the collision axis. After the collision, bore wave characteristics were observed over the less dense current, as in our case.

Unlike these previous case studies, this study emphasizes bore thermodynamics, inferred from the airborne Raman lidar. It is not easy to obtain airborne transects of colliding boundaries at the right time and place, and, in fact, the boundary collision observed on 8 June was a stroke of good luck. Because the collision occurred only 15 min after sunset, a significant SBL had not yet formed. The cold-frontal density current was slightly deeper (Fig. 6a) but less dense (~1.5 K higher θ_v, Fig. 6c) than the MCS outflow boundary: the average CRL-retrieved θ_v below 1.25 km MSL was 307.8 K in the cold-frontal density current (02:15 - 02:19 UTC, Fig. 6c), compared to 306.3 K in the MCS outflow (02:21 - 02:25 UTC). Fig. 6a suggests that the cold-frontal and MCS density currents were 850 m and 600 m deep, respectively. This has important implications

379 for bore formation following the collision because the MCS outflow was cooler and denser than
380 the cold frontal airmass. CRL data shown in Fig. 6 and discussed below indicate that the
381 collision proceeded as shown schematically in Fig. 1b and c; the cold-frontal airmass was
382 partially blocked by the shallower MCS outflow, triggering a northward moving bore within the
383 cold-frontal airmass.

384 Initial development of a bore occurs when a layer of air is blocked and deepens locally,
385 producing an interface known as a hydraulic jump (typically in liquid), where supercritical flow
386 slows and becomes subcritical relative to a gravity wave. In this case of colliding boundaries,
387 partial blocking by the MCS outflow deepened the cold-frontal airmass on the north side of the
388 collision point (Fig. 9a and b). The top of the cold-frontal density current (initially about 1.4 km
389 MSL) was lifted to about 3.0 km MSL (Fig. 6b). The blocking region extended close to 20 km
390 ahead of the MCS gust front (Fig. 10c). Furthermore, KICT Doppler velocity data (Fig. 3e-h)
391 suggest that the collision does not appear to impede the momentum of the relatively deeper cold-
392 frontal airmass, at least not for a while, because this airmass continues moving southward over
393 the denser thunderstorm outflow. The elevated cold front is shown schematically at the left
394 (south) side of the transect of Fig. 10c, but it could be further south, in the area not sampled by
395 the CRL. By 03:23 UTC, a singular wave with small undulations has developed ahead of the
396 intruding MCS outflow, on top of the moist cold-frontal air (Fig. 10f and g). This is preceded (in
397 space, to the north) by a peak in vertical motion at flight level (Fig. 10e). By the time of the next
398 UWKA transect (not shown), this first gravity wave has advanced northward, and the maximum
399 vertical velocity exceeded 2 m s^{-1}.

400 The partial blocking of the cold-frontal airmass can be further investigated using the two-
401 layer hydraulic theory initially applied by Rottman and Simpson (1989). In their laboratory

experiments, the non-dimensional parameters, Froude number (*Fr*), and normalized height ratio (*D*) were able to describe the resulting flow regime and estimate bore strength. The Froude number is the ratio of the speed of a density current (C_{dc}) to the speed of a gravity wave (C_{gw}). The height ratio D compares the height of the obstacle (d_o) to the initial depth of the blocked fluid (h_o).

$$Fr = \frac{U}{\sqrt{g'h_0}} = \frac{C_{dc}}{C_{gw}} \quad (1)$$

$$\mathrm{D} = \frac{d_o}{h_o} \quad (2)$$

The relation between *Fr* and *D* determines the flow regime, i.e., whether a flow is blocked and forms a bore. For this application, the MCS outflow is acting as the blocking mechanism (lower layer obstacle). However, it is also moving in opposition to the cold-frontal airmass that is lifted over it. The speed of the cold-frontal density current (C_{dc}) relative to the obstacle is therefore the sum of their two speeds, 13.5 m s^{-1} in this case (the cold front speed: 5.7 $m\ s^{-1}$; outflow speed: 8.8 $m\ s^{-1}$). The speed of gravity wave in SBL can be calculated using the following equation (Klemp et al. 1997):

$$C_{gw} = \sqrt{g'h_o} = \sqrt{g\frac{\Delta\theta_v}{\theta_v}h_0} \quad (3)$$

The theoretical gravity wave speed (C_{gw}) is 6.4 m s^{-1} calculated from the CRL θ_v transect (Fig. 5c; θ_v: 307.8 K → 306.3 K) with cold-frontal airmass height (h_o) of 850 m and results in a Froude number of 2.11. The second parameter, the ratio of the height of the obstacle, i.e. the MCS outflow boundary (d_o = 600 m), to h_o is only 0.71 (Fig. 4c). The Froude number and the non-dimensional obstacle height indicate that the cold-frontal airflow is partially blocked, notwithstanding the unusually shallow MCS outflow. The bore strength *S* is defined as $S=h_1/h_o$,

where h_1 is the after-blocking depth. In this case, 2 < S < 3, which indicates that the bore is mostly undular with some turbulent mixing on the downstream faces (Simpson 1987).

Bore maintenance requires the presence of a wave duct, or at least some mechanism for wave energy reflectance and wave trapping (Crook 1988). Such wave trapping depends on the profile of the Scorer parameter, defined as:

$$l^2 = \frac{N^2}{(U-C)^2} - \frac{\frac{\partial^2 U}{\partial z^2}}{(U-C)^2} \qquad (4)$$

where l^2 represents the Scorer parameter, N^2 is Brunt-Vaisala frequency, U is the environmental wind speed normal to the direction of bore movement, C is the speed of a bore, and z is the vertical distance. The Scorer parameter was calculated using vertically interpolated MP1 radiosonde data (50 m vertical interval, Fig. 4a). A Scorer parameter decreasing rapidly with height to near-zero values indicates a favorable environment for wave trapping and bore maintenance (Crook 1998). In this case, the bore's wave energy emanates from about 2.2 km, located between layers of negative Scorer parameter near 2.0 and 2.5 km MSL (Fig. 4a). Bores typically propagate southward in the Great Plains, into the low-level jet, which acts to reflect wave energy (Haghi et al. 2017). The post-frontal environment in this case lacked a low-level jet. The southerly shear peaking at the top of the cold air mass (near 1.3 km MSL, Fig. 4a) resulted in a minimum in l^2 at 1.3 km through the curvature term in l^2 (second term on the right of equation 4). That level likely served as the base of the duct for a northward moving bore.

5.2 Solitary wave train

After the UWKA witnessed the initial collision (Fig. 6), blocking, and a solitary wave (Fig. 9), the aircraft followed the wave train north and conducted a 2nd racetrack pattern to monitor the evolving wave structure. The UWKA transects were oriented NNW to SSE to be

perpendicular to the waves as seen on radar (Fig. 9). On leg 1 of racetrack 2 (0357 UTC, Fig. 11a), as many as four to five waves had developed and were most apparent in LSR and flight-level vertical velocity and pressure perturbations. The first two waves appear to have similar amplitudes of around 500 meters (determined by following the variation the top of the cold front air in LSR) and similar perturbations in vertical velocity and pressure (Fig. 11a, b, c, and d). The trailing waves decreased in amplitude in a manner similar to a solitary wave train or soliton (Knupp 2006). The LSR cross-sections plainly show soliton devolvement occurring behind the bore (in reference of the northward movement of bores) above the partially blocked region. Note the quadrature phase shift between vertical velocity *w* and pressure perturbation *p'* in Fig. 11a and 11e. Interestingly, when the UWKA flew below the wave system in the cold-frontal airmass (Fig. 11a), the pressure ridges trailed the updrafts, indicating that the p' variations were primarily dynamic, as revealed in Grasmick et al. (2018); however, when the UWKA flew above the wave system in the residual layer (Fig. 11b, showing the next leg some 10 min later), the pressure ridges led the updrafts, which likely resulted from a combination of dynamic and hydrostatic forces. According to linear wave theory, purely hydrostatic forcing dictates that *w* and *p'* vary in phase.

Lidar attenuation is occurring at the crest of each wave, indicating the presence of clouds. Behind the last wave, a nearly continuous cloud layer existed (bottom panels in Fig. 11). In the next two flight transects, clouds thicken further in the upper reaches of the cold-frontal airmass, especially toward the rear of the wave train, and the leading wave began to dissipate (not shown). In leg 1 and 2 of racetrack 2 (Fig.11), substantial clouds were present, making Raman lidar retrieval questionable. Even so, flight-level vertical velocity and pressure perturbations retained four to five waves.

As the wave train continued northward, it moved over the surface meteorology vehicle MP1 (stationary during the IOP) (Fig. 9c and d). The wave train passage at MP1 was most notable in wind speed and direction (Fig. 12). The observations depict a regular interval of wind speed peaks occurring with a period that decreases from about 20 minutes between the first two waves to 12-15 minutes between the last apparent waves. Like the UWKA observations, these also display a soliton-like structure in that the amplitude of the wind maximum decreased with each successive wave. The wind direction shows some pattern of regularity as well, at least across the earlier, larger waves. Upon the outflow arrival (at about 03:45 UTC), wind direction shifted from northerly to southerly. At about the same time, pressure rose and temperature increased, followed by a quasi-static air density as expected from a bore (Koch et al. 1991), since the bore deepened and mixed the stratified air within the cold-frontal air. Following the passage of the first wave, the wind direction briefly returned to northerly by completing a 360° rotation counterclockwise. A similar wind turning pattern was repeated for the second wave, but the transition was less wave-like. After this, subsequent lower amplitude waves did not cause such dramatic wind shifts. Finally, analysis of the pressure in Fig. 11e reveals primarily a hydrostatic response; embedded in the rising trend are p' perturbations that match the wave structure in the wind.

Instrumentation at MP1 also included an upward-pointing Atmospheric Emitted Radiance Interferometer (AERI), whose data were used to retrieve temperature (Fig. 13a) and mixing ratio (Fig. 13b) profiles during soliton passage. Vertical motion associated with convergence and updrafts are highlighted as adiabatic cooling in the temperature field and moisture transport in the mixing ratio field. Two features stand out from the time-height cross-sections and θ_v contours. First, what appears to be a large-amplitude wave (just after 0230 UTC) was most

likely a short-lived updraft that coincidentally passes overhead. Radar loops (not shown) display a small region of weak echoes drifted over the site at this time. Although likely non-precipitating, the convergence of BL particles beneath the updraft was sufficient for radar detection. This updraft does not appear to be related to any convergence boundary but may have been initiated by the cold front passage about an hour earlier. Second, the deepening of the moister, slightly cooler cold-frontal air at 0345 UTC marked the arrival of the bore, whose depth (~2.0 km) generally matched LSR estimates (Fig. 10). Numerous waves follow the deepening; they appeared on scanning radar as multiple, parallel fine lines. Behind the bore, cooling occurred above the cold-frontal airmass, where the air was mixed upward and cooled adiabatically (dry or moist depending on the presence of clouds). Near the surface, cooling occurred on account of the cold front and MCS outflow arriving (e.g. 306 K θ_v contour).

6. Summary and discussion

The key findings of this case study, based on the 8 June 2015 IOP during PECAN, are as follows:

- This study demonstrates how the airborne CRL, in combination with proximity operational radar data and radiosonde data, can be used to characterize the fine-scale thermodynamic vertical structure and convective potential of colliding boundaries, to detail the horizontal and vertical extent of the plume of high θ_e air rising in the collision, and to track resulting bore formation and evolution.
- The case illustrates fine-scale storm and environment interactions that trigger deep convection. The "zipper-like" coalescence of an MCS outflow and a cold front led to

514 enhanced convergence ahead of the collision point, leading to the removal of CIN, observed
515 by the CRL, and to deep convection.
516 • Critical in this analysis are the CRL-based 2D cross-sections (time-height) of temperature,
517 humidity, and derived convective parameters (CAPE, CIN, parcel-specific distance to
518 LCL/LFC). These transects revealed elevated CAPE with little CIN in the intermediate
519 airmass lifted by the two converging density currents, resulting in short-lived deep
520 convection upon collision. Although, the cold frontal and outflow air masses both contained
521 large CIN, the cold frontal air needed less lift to reach its LFC. The CRL thermodynamic
522 data, as well as the lidar-derived aerosol scattering ratio available above and below flight
523 level, show that the collision pushed the less dense, pre-frontal air, possibly mixed with post-
524 frontal air, upward, generated a rising plume of high water vapor and aerosol that reached its
525 LFC and initiated convection.
526 • The collision between the cold front and outflow produced a bore on top of the cold-frontal
527 airmass, in the opposite direction of the cold front. The depth, propagation speed, and density
528 differences of the two boundary-layer fluids (the cold-frontal airmass and the denser MCS
529 outflow) suggest that the former was partially blocked, according to the two-layer hydraulic
530 theory initially applied by Rottman and Simpson (1989). The resulting bore initially
531 appeared as a singular wave (triggering deep convection), and then evolved into a soliton
532 evident on the radar as multiple, parallel fine lines. This soliton propagated northward over
533 the cold-frontal airmass and persisted for at least 3 hours after the collision.
534
535 This observational study describes the fine-scale thermodynamic vertical structure of the
536 collision between two relatively weak boundaries, one associated with a cold front, the other

with a MCS outflow. To our knowledge, this study is unprecedented in that it described the thermodynamic structure of convergent boundaries, resulting in CI, and of an undular bore propagating over the less dense airmass (the cold frontal surface). This analysis complements published density current collision case studies, which primarily present radar kinematic analyses and lack detailed thermodynamic information. This novel thermodynamic analysis is a powerful tool to assess convective potential and the structure of the collision boundary to improve the knowledge of small-scale CI generation and boundary evolution.

Acknowledgments. This study was funded by the National Science Foundation (NSF) Grant AGS-1359645. Guo Lin and Zhien Wang's effort is also supported by NSF Grant AGS-1917693 and NASA 80NSSC20K0663. This work benefitted from the hard work of the many PECAN participants who spent the night of 7-8 June 2015 collecting the data that made this study possible. PECAN data are provided by NCAR/EOL, which is funded by NSF. The authors would like to thank David Turner for providing AERI data. The authors would also like to acknowledge Chun Zhang for generating Fig. 1.

Data availability statement. The CRL, in situ, and surface-based data are available from PECAN EOL website (https://data.eol.ucar.edu/master_lists/generated/pecan/)

556 **Reference**
557

558 Blake, B. T., D. B. Parsons, K. R. Haghi, and S. G. Castleberry, 2017: The Structure, Evolution,
559 and Dynamics of a Nocturnal Convective System Simulated Using the WRF-ARW
560 Model. *Mon. Wea. Rev.*, **145**, 3179–3201, https://doi.org/10.1175/MWR-D-16-0360.1.

561 Clarke, R.H., 1972: The morning glory: an atmospheric hydraulic jump. J. Appl. Meteor., **11**,
562 304-311, https://doi.org/10.1175/1520-0450(1972)011<0304:TMGAAH>2.0.CO;2.

563 Corfidi, S. F., S. J. Corfidi, and D. M. Schultz, 2008: Elevated Convection and Castellanus:
564 Ambiguities, Significance, and Questions. *Wea. Forecasting*, **23**, 1280–
565 1303, https://doi.org/10.1175/2008WAF2222118.1.

566 Crook, N. A., 1988: Trapping of Low-Level Internal Gravity-Waves. *J. Atmos. Sci.*, **45,** 1533-
567 1541, https://doi.org/10.1175/1520-0469(1988)045<1533:Tollig>2.0.Co;2

568 Crum, T.D., Alberty, R.L. and Burgess, D.W., 1993: Recording, archiving, and using WSR-88D
569 data. *Bull. Amer. Meteor. Soc*, **74**, 645-654, https://doi.org/10.1175/1520-
570 0477(1993)074<0645:RAAUWD>2.0.CO;2

571 Droegemeier, K. K., R. B. Wilhelmson, 1985: Three-Dimensional Numerical Modeling of
572 Convection Produced by Interacting Thunderstorm Outflows. Part I: Control Simulation
573 and Low-Level Moisture Variations. *J. Atmos. Sci.,* **42**, 2381-2403,
574 https://doi.org/10.1175/1520-0469(1985)042<2404:TDNMOC>2.0.CO;2

575 Frank, P.J. and Kucera, P.A., 2003, August. Radar characteristics of convection along colliding
576 outflow boundaries observed during CRYSTAL-FACE. In *Preprints, 31st Int. Conf. on*
577 *Radar Meteorology, Seattle, WA, Amer. Meteor. Soc. A* (Vol. 12).

578 Geerts, B., R. Damiani, and S. Haimov, 2006: Finescale Vertical Structure of a Cold Front as
579 Revealed by an Airborne Doppler Radar. *Mon. Wea. Rev,* **134**, 251-271,
580 https://doi.org/10.1175/MWR3056.1.
581 Geerts, B., and Coauthors, 2017: The 2015 Plains Elevated Convection at Night Field
582 Project. *Bull. Amer. Meteor. Soc.*, **98**, 767-786, https://doi.org/10.1175/BAMS-D-15-
583 00257.1.
584 Geerts, B. and Miao, Q., 2005. Airborne radar observations of the flight behavior of small insects
585 in the atmospheric convective boundary layer. *Environ. Entomol.*, **34**, 361-377,
586 https://doi.org/10.1603/0046-225X-34.2.361
587 Grasmick, C., B. Geerts, D. D. Turner, Z. Wang, and T. M. Weckwerth, 2018: The Relation
588 between Nocturnal MCS Evolution and Its Outflow Boundaries in the Stable Boundary
589 Layer: An Observational Study of the 15 July 2015 MCS in
590 PECAN. *Mon.Wea.Rev.,* **146**, 3203-3226, https://doi.org/10.1175/MWR-D-18-0169.1.
591 Haghi, K. R., D. B. Parsons, and A. Shapiro, 2017: Bores Observed during IHOP_2002: The
592 Relationship of Bores to the Nocturnal Environment. *Mon. Wea. Rev.,* **145**, 3929-3946,
593 https://doi.org/10.1175/MWR-D-16-0415.1.
594 Haghi, K.R., and Coauthors, 2019: Bore-ing into nocturnal convection. *Bull. Amer. Meteor. Soc*.,
595 **100,** 1103-1121, https://doi.org/10.1175/BAMS-D-17-0250.1.
596 Harrison, S. J., J. R. Mecikalski, and K. R. Knupp, 2009: Analysis of Outflow Boundary
597 Collisions in North-Central Alabama. *Wea. Forecasting*, **24,** 1680-1690,
598 https://doi.org/10.1175/2009waf2222268.1

599 Intrieri, J. M., A. J. Bedard, and R. M. Hardesty, 1990: Details of Colliding Thunderstorm
600 Outflows as Observed by Doppler Lidar. *J. Atmos. Sci.,* 47, 1081-1099,
601 https://doi.org/10.1175/1520-0469(1990)047<1081:DOCTOA>2.0.CO;2.
602 Johnson, A., and X. Wang, 2019: Multicase Assessment of the Impacts of Horizontal and
603 Vertical Grid Spacing, and Turbulence Closure Model, on Subkilometer-Scale
604 Simulations of Atmospheric Bores during PECAN. *Mon. Wea. Rev.*, **147**, 1533–
605 1555, https://doi.org/10.1175/MWR-D-18-0322.1.
606 Karan, H., and K. Knupp, 2009: Radar and Profiler Analysis of Colliding Boundaries: A Case
607 Study. *Mon. Wea. Rev.,* **137**, 2203-2222, https://doi.org/10.1175/2008MWR2763.1.
608 Kingsmill, D. E., 1995: Convection Initiation Associated with a Sea-Breeze Front, a Gust Front,
609 and Their Collision. *Mon. Wea. Rev*, **123,** 2913-2933, https://doi.org/10.1175/1520-
610 0493(1995)123<2913:Ciawas>2.0.Co;2
611 Kingsmill, D. E., and N. A. Crook, 2003: An observational study of atmospheric bore formation
612 from colliding density currents. *Mon. Wea. Rev*, **131,** 2985-3002,
613 https://doi.org/10.1175/1520-0493(2003)131<2985:Aosoab>2.0.Co;2
614 Klemp, J. B., R. Rotunno, and W. C. Skamarock, 1997: On the propagation of internal bores. J.
615 Fluid Mech., **331**, 81–106, https://doi.org/10.1017/S0022112096003710.
616 Klein, P., et al. 2016: Mobile PISA 1 OU/NSSL CLAMPS Radiosonde Data. Version 1.0.
617 UCAR/NCAR - Earth Observing Laboratory, Accessed 26 Aug
618 2020, https://doi.org/10.5065/D6416VDH
619 Knupp, K., 2006: Observational analysis of a gust front to bore to solitary wave transition within
620 an evolving nocturnal boundary layer. *J. Atmos. Sci.*, **63**, 2016-2035,
621 https://doi.org/10.1175/JAS3731.1.

622 Knuteson, R. O., and Coauthors, 2004a: Atmospheric Emitted Radiance Interferometer. Part I:
623 Instrument design. *J. Atmos. Oceanic Technol.*, **21**, 1763–1776,
624 https://doi.org/10.1175/JTECH-1662.1.
625 Knuteson, R. O., and Coauthors, 2004b: Atmospheric Emitted Radiance Interferometer. Part II:
626 Instrument performance. *J. Atmos. Oceanic Technol.*, **21**, 1777–1789,
627 https://doi.org/10.1175/JTECH-1663.1.
628 Koch, S. E., P. B. Dorian, R. Ferrare, S. H. Melfi, W. C. Skillman, and D. Whiteman, 1991:
629 Structure of an Internal Bore and Dissipating Gravity Current as Revealed by Raman
630 Lidar. *Mon. Wea. Rev.,* **119**, 857-887, https://doi.org/10.1175/1520-
631 0493(1991)119<0857:Soaiba>2.0.Co;2
632 Lin, G., B. Geerts, Z. E. Wang, C. Grasmick, X. Q. Jing, and J. Yang, 2019: Interactions between
633 a Nocturnal MCS and the Stable Boundary Layer as Observed by an Airborne Compact
634 Raman Lidar during PECAN. *Mon. Wea. Rev.*, **147,** 3169-3189,
635 https://doi.org/10.1175/Mwr-D-18-0388.1
636 Liu, B., Wang, Z., Cai, Y., Wechsler, P., Kuestner, W., Burkhart, M. and Welch, W., 2014.
637 Compact airborne Raman lidar for profiling aerosol, water vapor and clouds. *Opt.*
638 *express*, **22**, 20613-20621, https://doi.org/10.1364/OE.22.020613
639 Loveless, D. M., T. J. Wagner, D. D. Turner, S. A. Ackerman, and W. F. Feltz, 2019: A
640 Composite Perspective on Bore Passages during the PECAN Campaign. *Mon. Wea.*
641 *Rev.*, **147**, 1395–1413, https://doi.org/10.1175/MWR-D-18-0291.1.
642 Martin, W.J. and A. Shapiro, 2007: Discrimination of Bird and Insect Radar Echoes in Clear Air
643 Using High-Resolution Radars. *J. Atmos. Oceanic Technol.,* **24**, 1215–1230,
644 https://doi.org/10.1175/JTECH2038.1

645 Miao, Q. and Geerts, B., 2007. Finescale vertical structure and dynamics of some dryline
646 boundaries observed in IHOP. *Mon. Wea. Rev.*, **135**, 4161-4184,
647 https://doi.org/10.1175/2007MWR1982.1
648 Miller, P.A., Barth, M.F., Benjamin, L.A., Artz, R.S. and Pendergrass, W.R., 2005: The
649 Meteorological Assimilation and Data Ingest System (MADIS): Providing value-added
650 observations to the meteorological community. In *Preprints, 21st Conf. on Weather*
651 *Analysis and Forecasting/17th Conf. on Numerical Weather Prediction, Washington, DC,*
652 *Amer. Meteor. Soc.*
653 https://ams.confex.com/ams/WAFNWP34BC/techprogram/paper_98637.htm
654 Mueller, D., B. Geerts, Z. Wang, M. Deng, and C. Grasmick, 2017: Evolution and Vertical
655 Structure of an Undular Bore Observed on 20 June 2015 during
656 PECAN. *Mon.Wea.Rev.,* **145**, 3775-3794, https://doi.org/10.1175/MWR-D-16-0305.1.
657 Parsons, D. B., K. R. Haghi, K. T. Halbert, B. Elmer, and J. Wang, 2019: The Potential Role of
658 Atmospheric Bores and Gravity Waves in the Initiation and Maintenance of Nocturnal
659 Convection over the Southern Great Plains. *J. Atmos. Sci.*, **76**, 43–
660 68, https://doi.org/10.1175/JAS-D-17-0172.1.
661 Peters, J. M., C. J. Nowotarski, and H. Morrison, 2019: The role of vertical wind shear in
662 modulating maximum supercell updraft velocities. *J. Atmos. Sci.*, **76**, 3169–3189,
663 https://doi.org/10.1175/JAS-D-19-0096.1.
664 Purdom, J., 1982: Subjective interpretation of geostationary satellite data for
665 nowcasting. *Nowcasting,* K. Browning, Ed., Academic Press, 149-166.
666 Roberts, R.D., Fabry, F., Kennedy, P.C., Nelson, E., Wilson, J.W., Rehak, N., Fritz, J.,
667 Chandrasekar, V., Braun, J., Sun, J. and Ellis, S., 2008: REFRACTT 2006: Real-time

retrieval of high-resolution, low-level moisture fields from operational NEXRAD and research radars. *Bull. Amer. Meteor. Soc.*, **89**, 1535-1548, https://doi.org/10.1175/2008BAMS2412.1.

Rottman, J. W., J. E. Simpson, 1989: The formation of internal bores in the atmosphere: A laboratory model. *Quart. J. Roy. Meteorol. Soc.,* **115**, 941-963, https://doi.org/10.1002/qj.49711548809.

Rotunno, R., J. B. Klemp, and M. L. Weisman, 1988: A Theory for Strong, Long-Lived Squall Lines. *J. Atmos. Sci.,* **45**, 463-485, https://doi.org/10.1175/1520-0469(1988)045<0463:Atfsll>2.0.Co;2

Russell, R.W. & Wilson, J.W: Boundary-Layer Meteorology (1997) 82: 235, https://doi.org/10.1023/A:1000237431851.

Simpson, J. E., 1987: Gravity Currents in the Environment and the Laboratory. Ellis Horwood Limited, 244 pp.

Turner, D. 2018. MP1 OU/NSSL CLAMPS AERIoe Thermodynamic Profile Retrieval Data. Version 1.2. UCAR/NCAR - Earth Observing Laboratory. https://doi.org/10.5065/D6VQ312C. Accessed 28 Dec 2020.

Turner, D.D. and U. Löhnert, 2014: Information content and uncertainties in thermodynamic profiles and liquid cloud properties retrieved from the ground-based Atmospheric Emitted Radiance Interferometer (AERI). *J. Appl. Meteor. Climatol.*, **53**, 752-771, https://doi.org/10.1175/JAMC-D-13-0126.1.

Turner, D. 2016: MP1 OU/NSSL CLAMPS MWR and Surface Meteorology Data. Version 1.0. UCAR/NCAR - Earth Observing Laboratory. https://doi.org/10.5065/D6707ZT3. Accessed 26 Aug 2020.

691 UCAR/NCAR - Earth Observing Laboratory. 2011. NOAA/ESRL/GSD MADIS Data including
692 MesoWest (netCDF format). Version 1.0. UCAR/NCAR - Earth Observing Laboratory.
693 https://data.eol.ucar.edu/dataset/100.001. Accessed 26 Aug 2020.
694 University of Wyoming - Flight Center, 2007: The University of Wyoming Cloud Lidar (WCL).
695 University of Wyoming, College of Engineering, Department of Atmospheric
696 Science, doi:10.15786/M25W9D.
697 Vermeesch, K. 2015. FP2 Greensburg, KS Radiosonde Data. Version 1.0. UCAR/NCAR - Earth
698 Observing Laboratory. https://doi.org/10.5065/D6FQ9TPH. Accessed 28 Dec 2020.
699 Wakimoto, R.M., 1982: The life cycle of thunderstorm gust fronts as viewed with Doppler radar
700 and rawinsonde data. *Mon. Wea. Rev*, **110**, 1060-1082, https://doi.org/10.1175/1520-
701 0493(1982)110<1060:TLCOTG>2.0.CO;2
702 Wakimoto, R. M., D. E. Kingsmill, 1995: Structure of an Atmospheric Undular Bore Generated
703 from Colliding Boundaries during CaPE. *Mon. Wea. Rev.,* 123, 1374-1393,
704 10.1175/1520- https://doi.org/0493(1995)123<1374:Soaaub>2.0.Co;2
705 Wakimoto, R.M., H.V. Murphey, E.V. Browell, and S. Ismail, 2006: The "Triple Point" on 24
706 May 2002 during IHOP. Part I: Airborne Doppler and LASE Analyses of the Frontal
707 Boundaries and Convection Initiation. *Mon. Wea. Rev.,* **134**, 231–250,
708 https://doi.org/10.1175/MWR3066.1
709 Wang, Z., 2020. Airborne Compact Raman Lidar (CRL) Water Vapor and Temperature Profiles.
710 Version 2.0. UCAR/NCAR - Earth Observing Laboratory.
711 https://doi.org/10.26023/JYNH-KCZE-910F. Accessed 08 Dec 2020.

712 Wang, Z., et al. 2016. University of Wyoming King Air Compact Raman Lidar Data. Version
713 1.0. UCAR/NCAR - Earth Observing Laboratory. https://doi.org/10.5065/D6MS3R0P.
714 Accessed 26 Aug 2020.
715 Wang, Z., Wechsler, P., Kuestner, W., French, J., Rodi, A., Glover, B., Burkhart, M. and Lukens,
716 D., 2009: Wyoming Cloud Lidar: instrument description and applications. *Opt. Express*,
717 **17,** 13576-13587, https://doi.org/10.1364/Oe.17.013576
718 Waugh, S., Ziegler, C. 2017. NSSL Mobile Mesonet Data. Version 1.1. UCAR/NCAR - Earth
719 Observing Laboratory. https://doi.org/10.5065/D64M92RG. Accessed 26 Aug 2020.
720 Weckwerth, T. M., and D. B. Parsons, 2006: A review of convection initiation and motivation
721 for IHOP_2002. *Mon. Wea. Rev.,* **134,** 5-22, https://doi.org /10.1175/Mwr3067.1.
722 Weckwerth, T. M., J. Hanesiak, J. W. Wilson, S. B. Trier, S. K. Degelia, W. A. Gallus, R. D.
723 Roberts, and X. Wang, 2019: Nocturnal Convection Initiation during PECAN 2015. *Bull.*
724 *Amer. Meteor. Soc.*, **100**, 2223–2239, https://doi.org/10.1175/BAMS-D-18-0299.1.
725 Wilson, J. W. and W. E. Schreiber, 1986: Initiation of Convective Storms at Radar-Observed
726 Boundary-Layer Convergence Lines. *Mon. Wea. Rev.,* **114**, 2516-2536,
727 https://doi.org/10.1175/1520-0493(1986)114<2516:IOCSAR>2.0.CO;2
728 Wu, D., Z. Wang, P. Wechsler, N. Mahon, M. Deng, B. Glover, M. Burkhart, W. Kuestner, and
729 B. Heesen, 2016: Airborne compact rotational Raman lidar for temperature
730 measurement. *Opt. Express*, **24**, A1210-A1223, https://doi.org/10.1364/OE.24.0A1210.
731

732 **Figures**

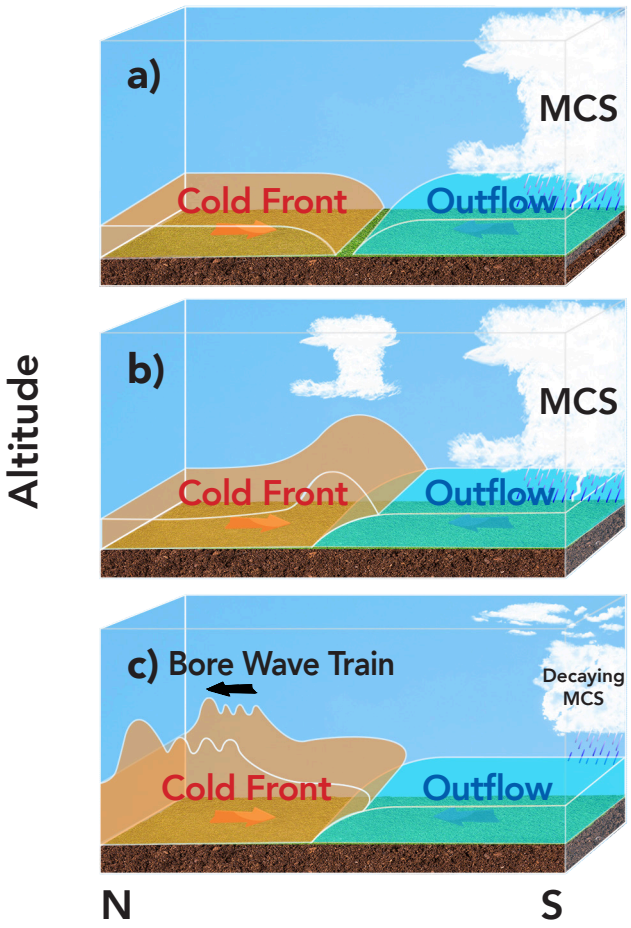

733

734 **Fig. 1:** (a) Conceptual 3D view of the collision between the cold front and the MCS outflow in
735 this case study; (b) as they collide, shallow to deep convection results; (c) a bore emerges from
736 the cold-frontal bulge and propagates in the same direction as the denser MCS outflow.

737

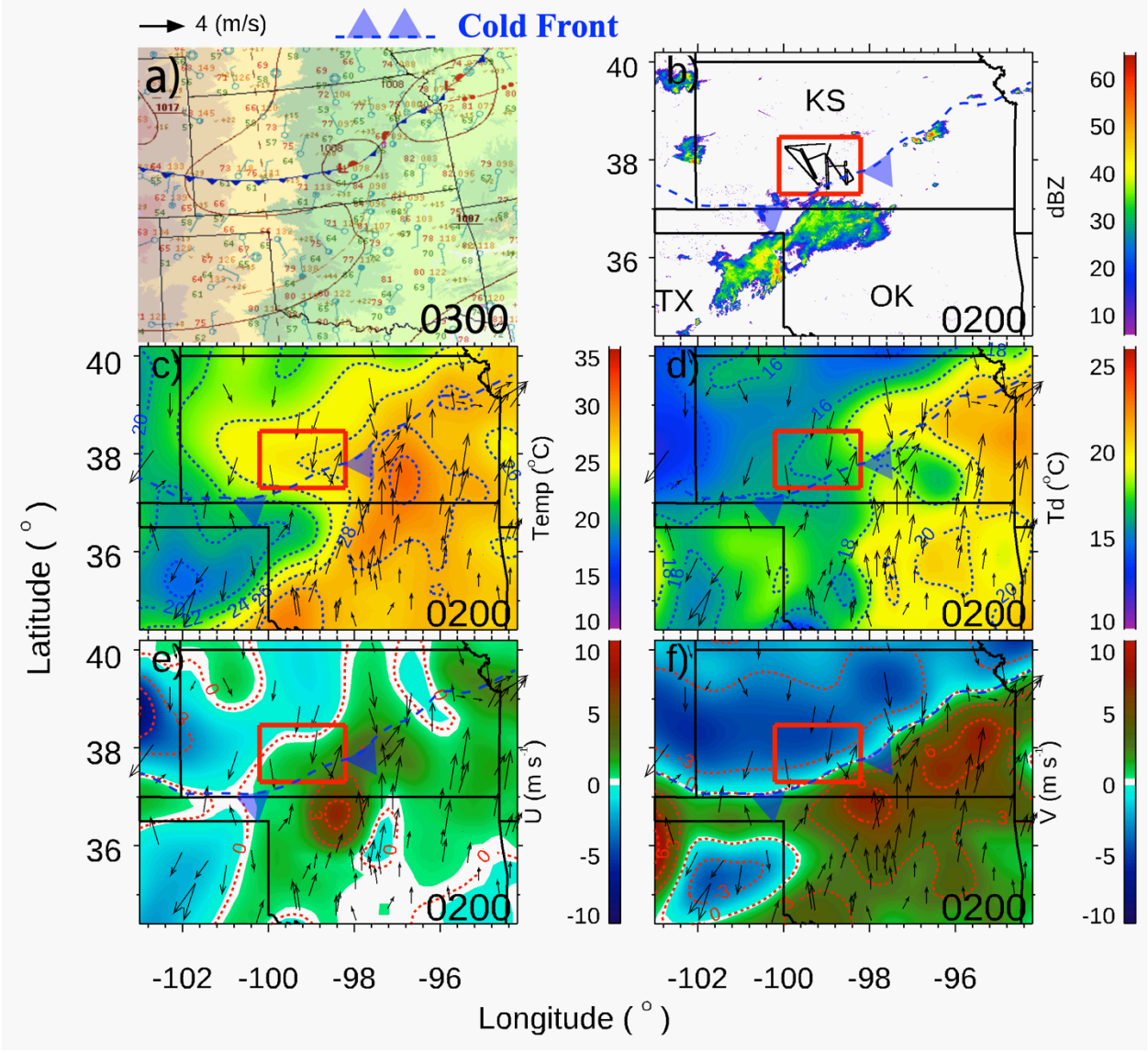

738

739 **Fig. 2:** (a) The surface analysis map from Weather Prediction Center at 0300 UTC; (b)

740 NEXRAD 3D mosaic radar image at the height of 3.0 km and 0200 UTC and the total UWKA

741 flight track; interpolated MADIS surface (c) temperature, (d) dewpoint, (e) zonal wind; and (f)

742 meridional wind with wind vectors from irregular distribution MADIS data at 0200 UTC.

743

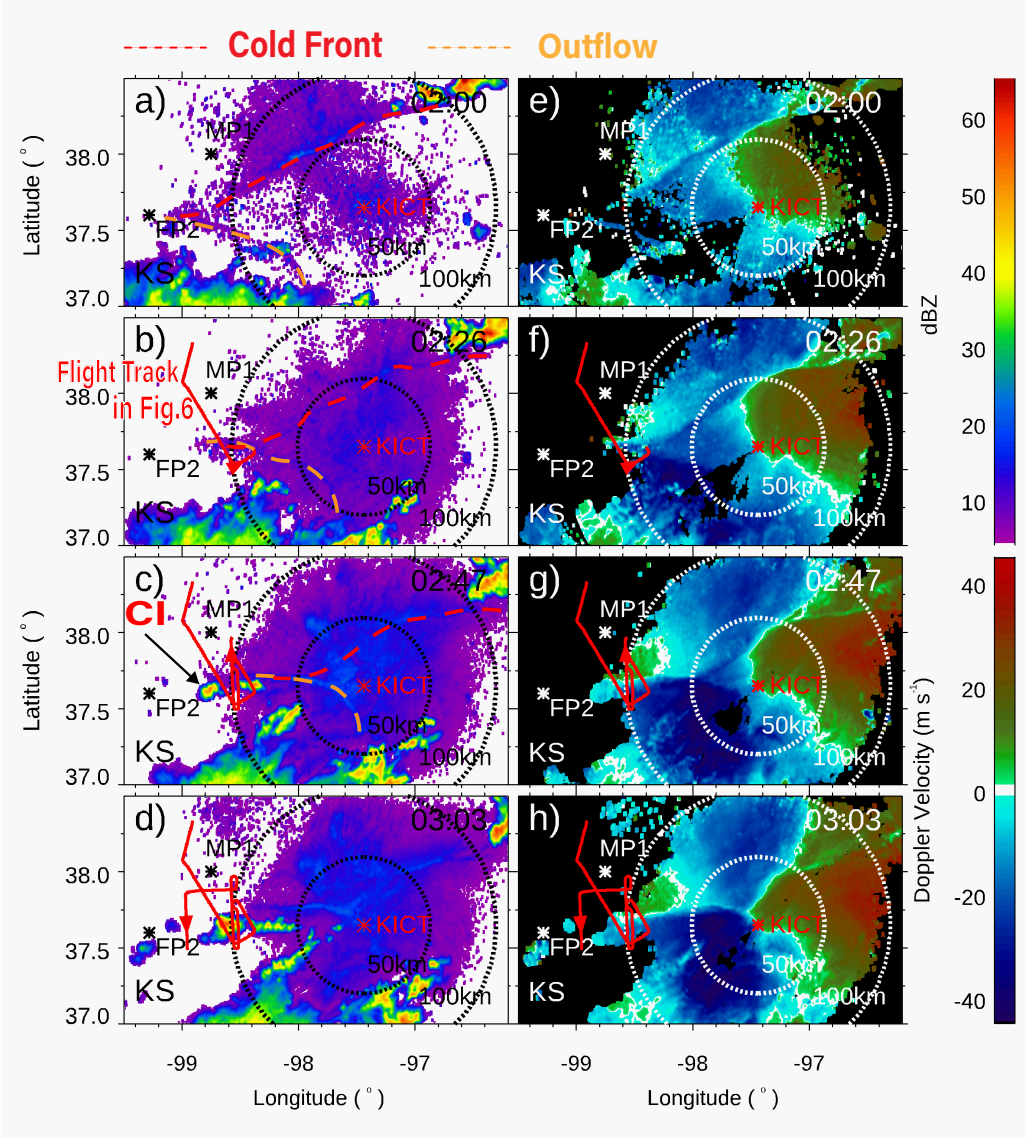

744

745 **Fig 3:** Smoothed NEXRAD KITC base reflectivity (dBZ) maps with UWKA flight track (the red
746 solid line represents the flight-path within the last 20-30 minutes, red dashed line represents cold
747 front, and orange dashed line represents outflow from parent MCS) at (a) 0200, (b) 0226, (c)
748 0247, (d) 0303 UTC on 8 June 2015; KICT base-level Doppler velocity ($m\ s^{-1}$) (positive away
749 from the radar). The increasing distance of UWKA flight track (red solid line) is the flight
750 between the last panel to the corresponding time.

751

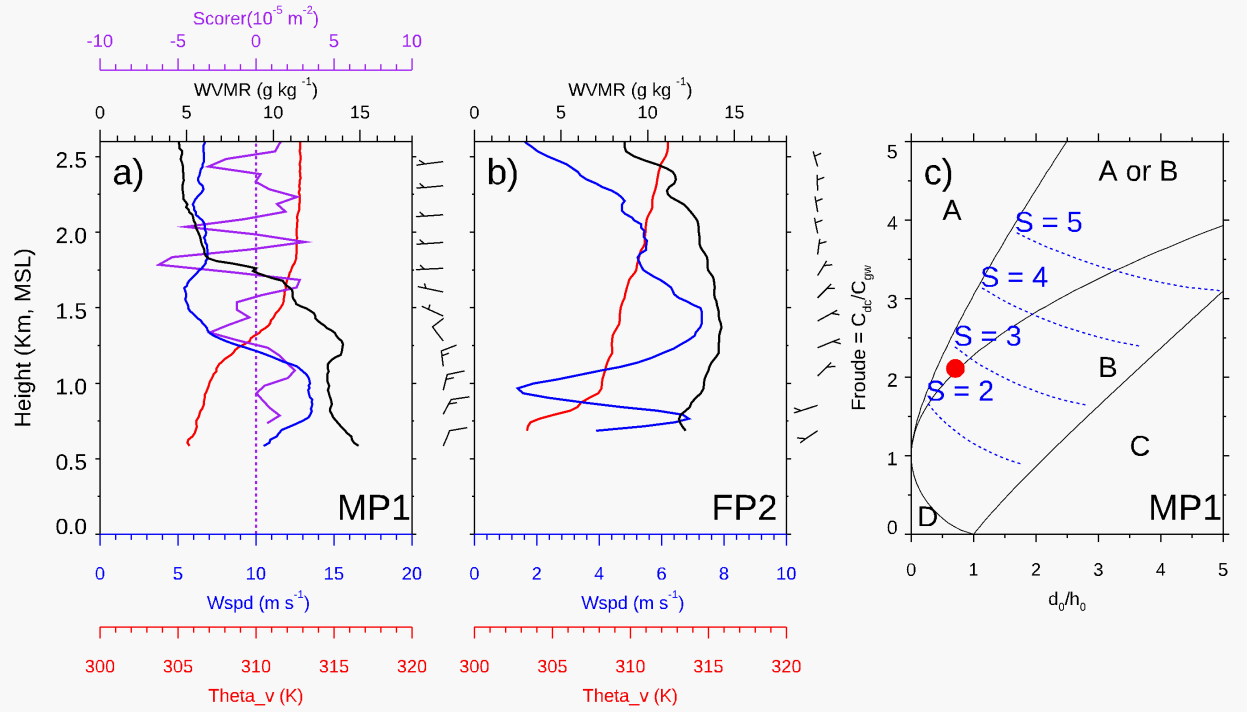

Fig. 4. (a) MP1 radiosonde profiles of WVMR (black), environment wind speed (blue), virtual potential temperature (red), scorer number (purple), and wind bars; (b) FP2 radiosonde profiles of WVMR (black), environment wind speed (blue), virtual potential temperature (red), and wind bars; (c) bore flow regimes adapted from Knupp (2006), with regime boundaries (black solid lines) based on Rottman and Simpson's (1989) hydraulic theory. The abscissa is the normalized density current depth d_0/h_0, and the ordinate is the Froude number. The blue dotted lines delineate bore strength S. The red dot is the calculated flow regime value for the outflow boundary around 0306 UTC.

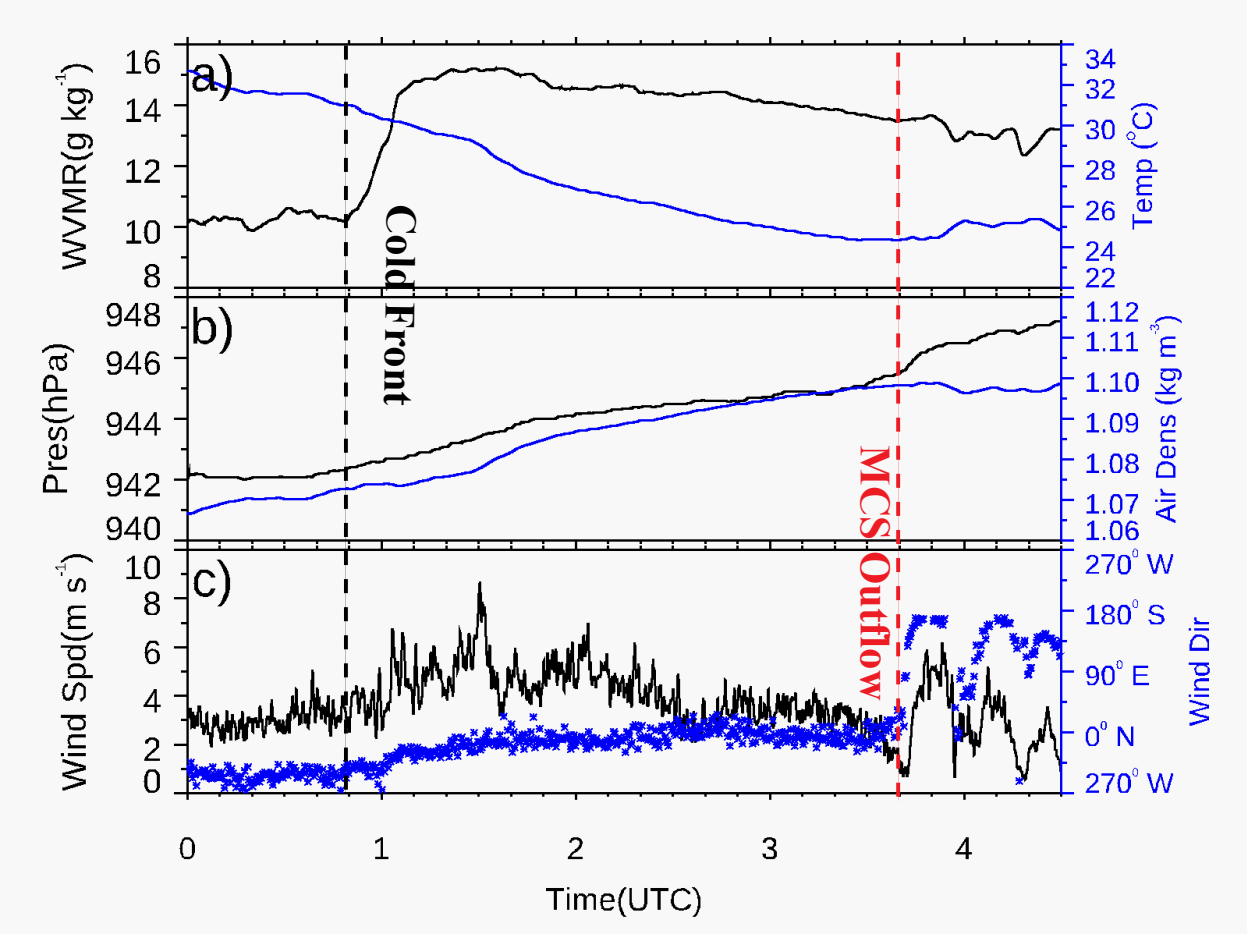

763

764

765 **Fig. 5.** (a) Surface WVMR (black) and temperature (blue), (b) surface pressure (black) and air

766 density (blue), and (c) the 2m wind speed (black) and wind direction (blue) from MP1.

767

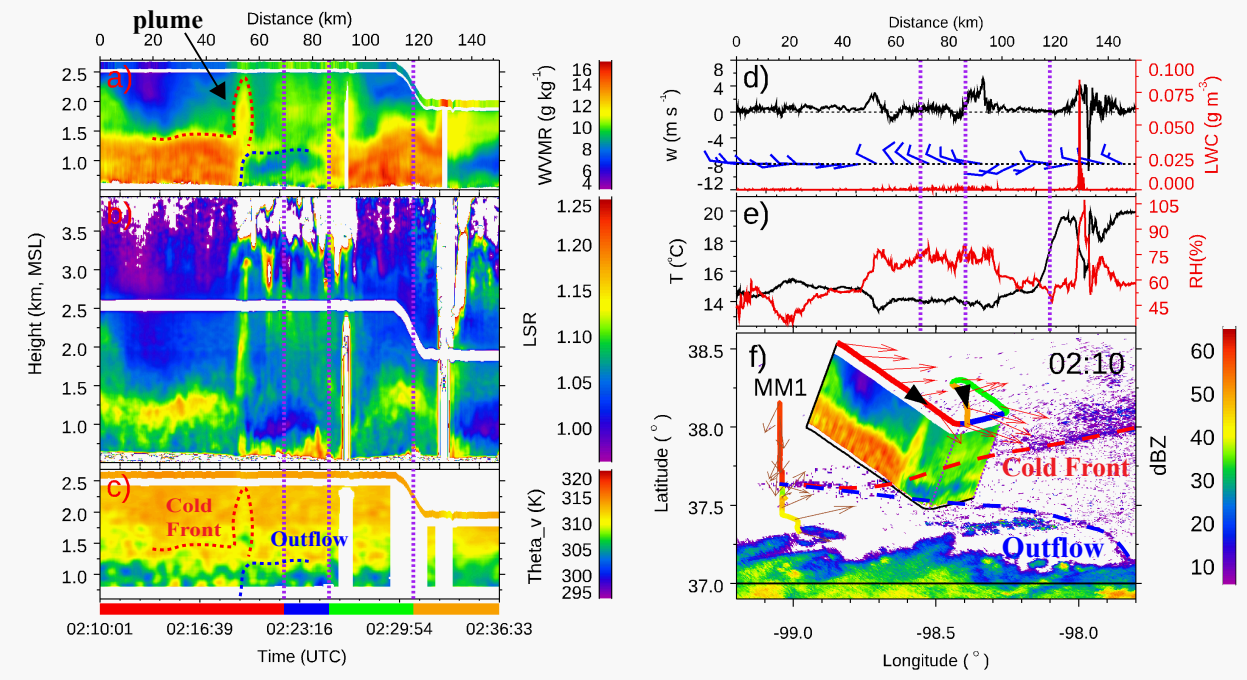

768

769 **Fig. 6:** Analysis of flight legs 1-4. The four different colors below the time-axis of the left panel
770 and on the map in panel (f) represent these 4 legs, and the 4 legs are shown in Fig. 3. The vertical
771 dashed lines across panels represent aircraft turns between legs; (a) the flight-level in situ
772 WVMR and CRL WVMR between flight level and the ground, (b) lidar scattering ratio (LSR)
773 below and above flight level, and (c) the flight-level in situ virtual potential temperature and
774 CRL's derived virtual potential temperature (the red dashed line marks cold front, and blue
775 dashed line marks outflow); (d) flight-level air vertical velocity, LWC, and horizontal wind (a
776 full wind barb represents 10 $m\ s^{-1}$); (e) flight level temperature and relative humidity. The flight
777 level is 2.4 km MSL in legs 1-3, and 1.8 km MSL in leg 4. (f) the flight track, horizontal wind
778 vectors at flight level, CRL WVMR transect (first two legs only), surface mesonet (MM1)
779 detected WVMR and wind (driving south between 02:12-03:15 UTC), and the KITC base
780 reflectivity at 02:10 UTC.

781

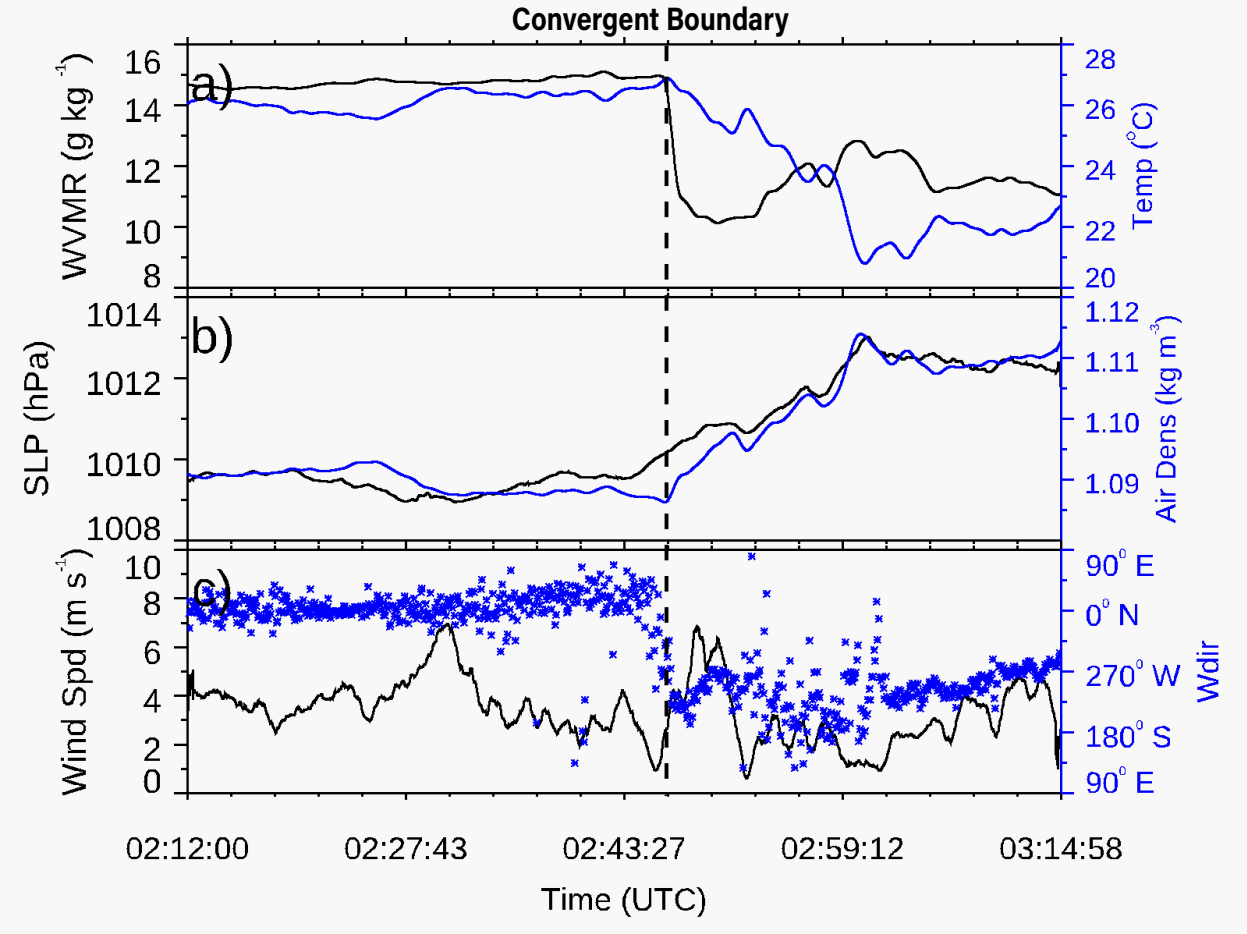

782

783 **Fig. 7:** 1 Hz meteorological data from MM1 driving south (track shown in Fig. 6f): (a) WVMR
784 (black solid line) and temperature (blue solid line), (b) the sea level pressure (black solid line)
785 and air density (blue solid line), and (c) the 2m wind speed (black solid line) and the wind
786 direction (blue dots).

787

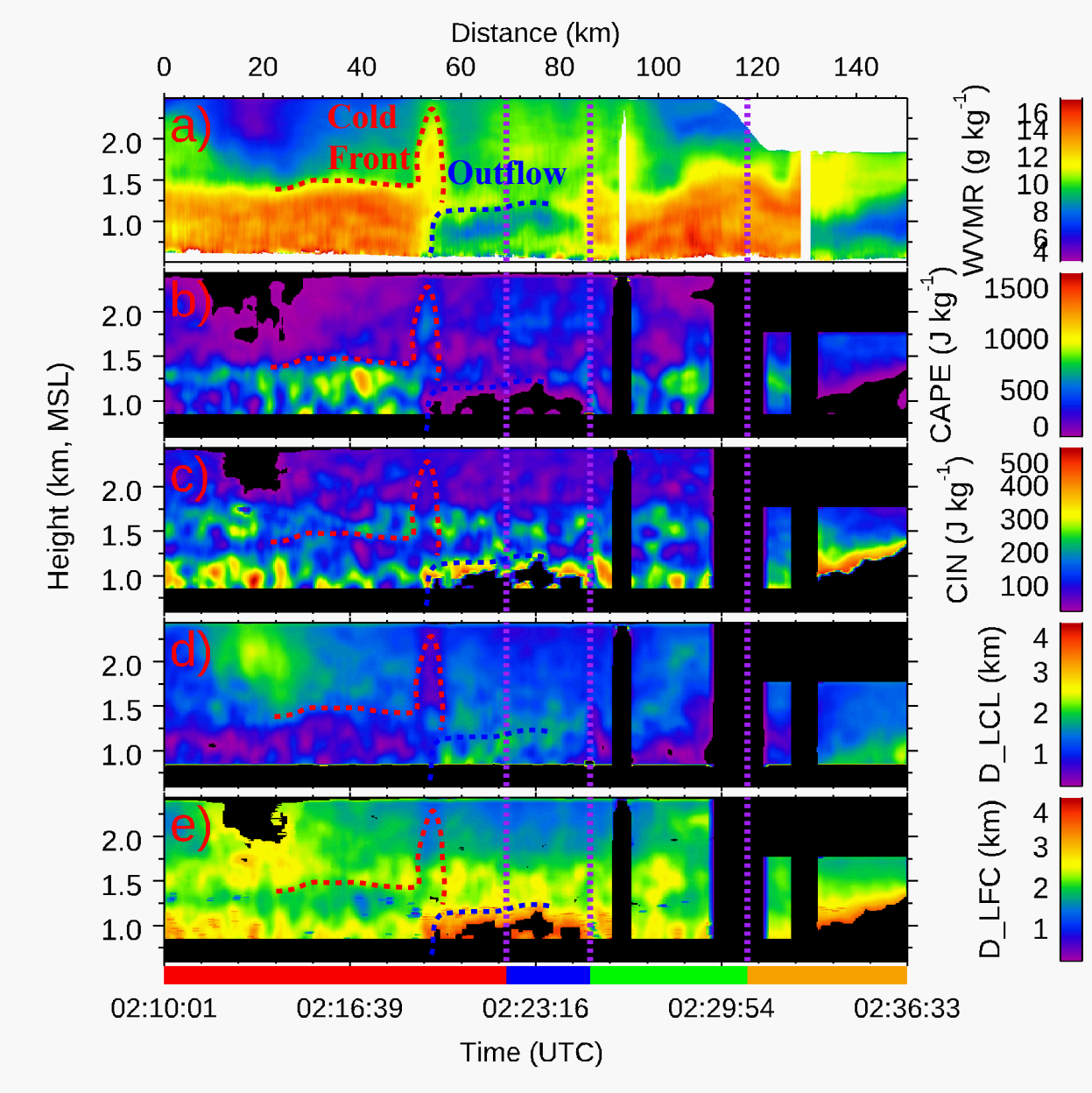

788

789 **Fig. 8:** (a) the CRL WVMR between flight level and the ground, (b) CRL-derived CAPE, (c)

790 CIN, (d) distance to LCL, and (e) distance to LFC calculated from the re-construct sounding

791 between the CRL data and MP1 radiosonde data at 03:06 UTC.

792

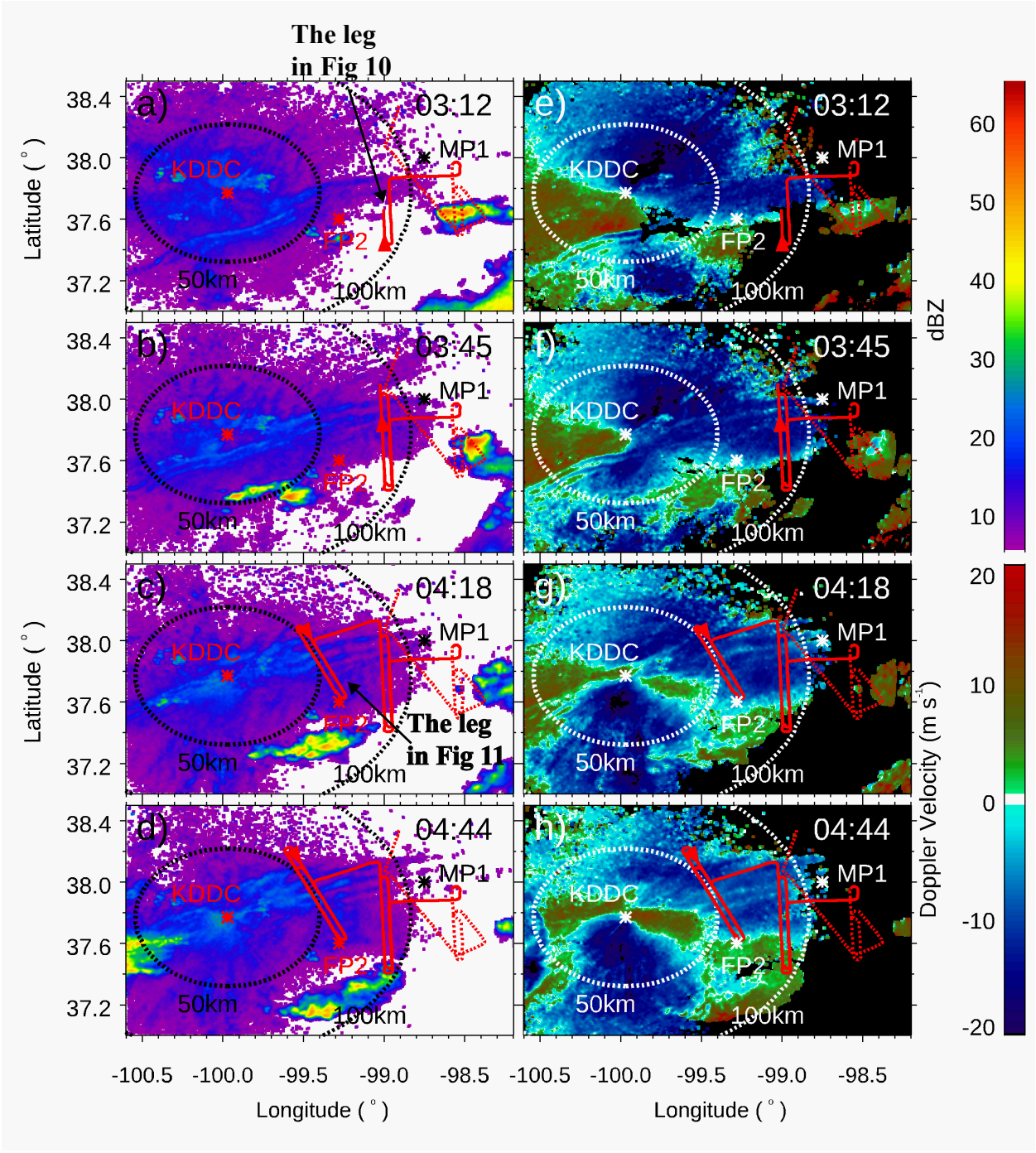

793

794 **Fig. 9**: As Fig. 3, but using the KDDC radar data at (a) and (e) 03:12, (b) and (f) 03:45, (c) and

795 (g) 04:18, (d) and (h) 04:44 UTC. The red dashed lines represent the earlier flight track. The

796 solid red flight tracks in (a) and (e) are the time period between 02:47 (the radar time in Fig. 3c)

797 to 03:45 UTC.

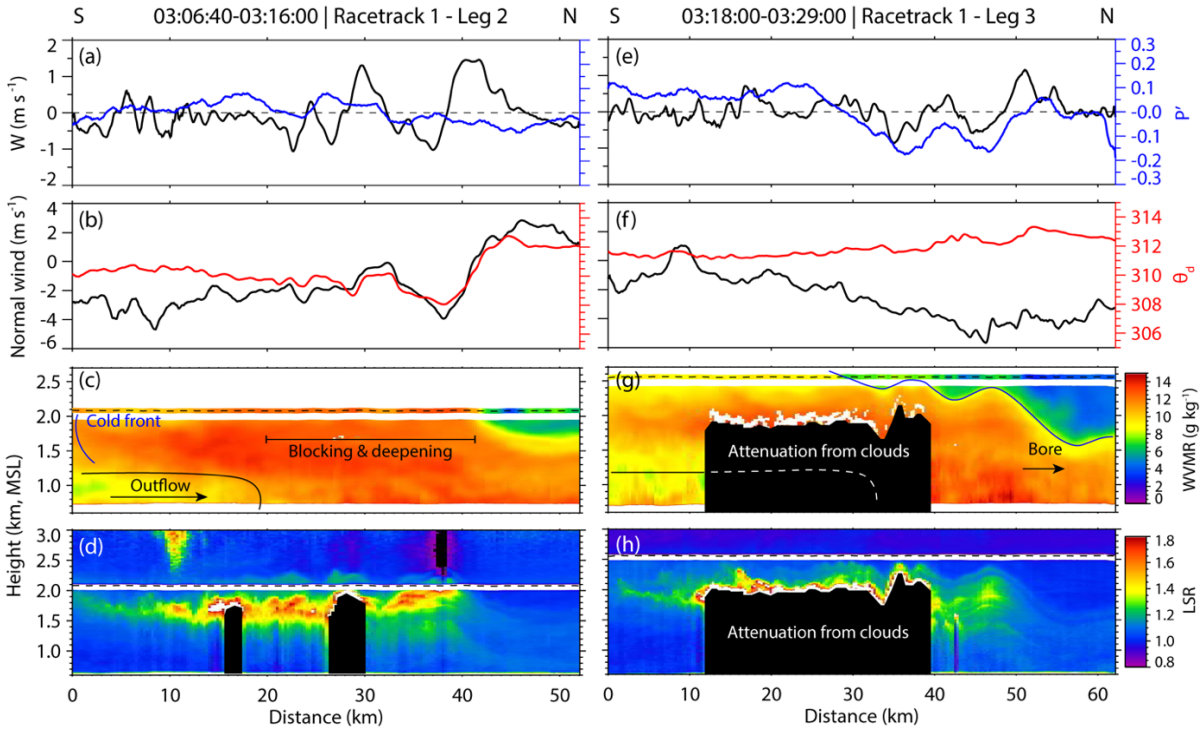

798

Fig 10: UWKA flight level data and CRL cross-sections from race track 1, legs 2 and 3 (located in Fig. 9) showing the blocking of the post-frontal air mass and the development of the first wave. (a) and (e) flight-level air vertical velocity and perturbation pressure *p'*, (b) and (f) flight-level bore-relative wind speed (negative means slower than the bore, i.e. front-to-rear), and virtual potential temperature. The flight level is 2.0 km MSL. (c) and (g) CRL and in situ (thin lines above the white gap) WVMR, (d) and (h) LSR from the up and down pointing lidars with middle white gaps indicating flight levels.

799

800

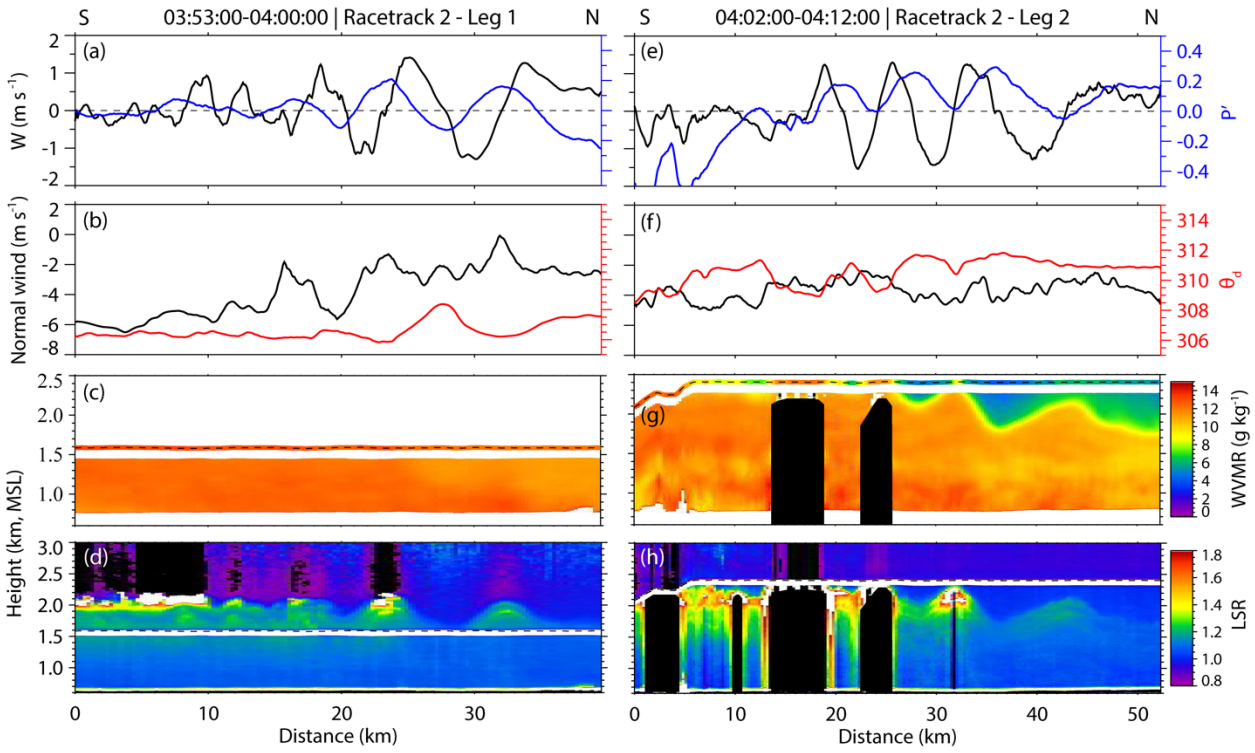

801

802 **Fig. 11:** As Fig. 10, but for race track 2.

803

804

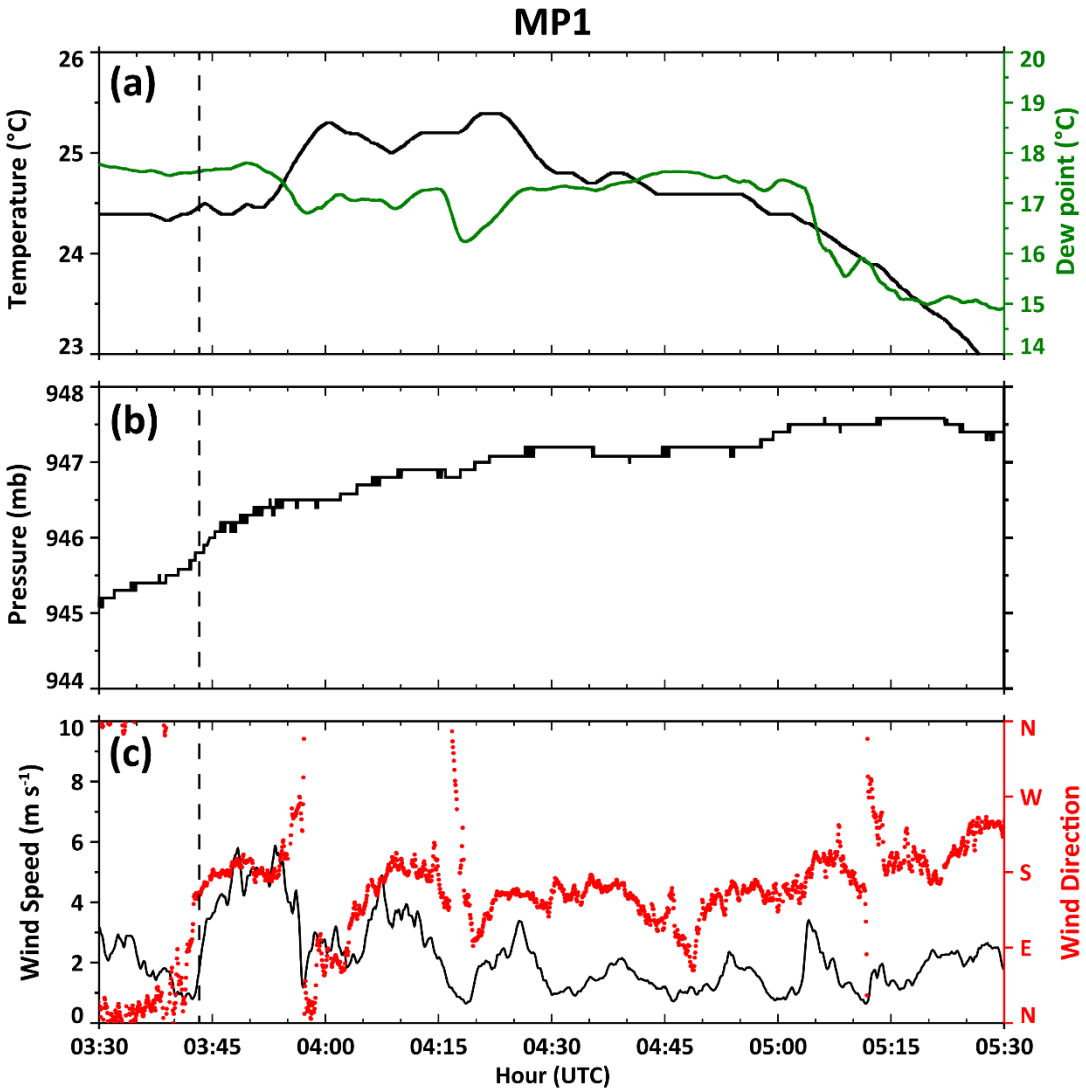

Fig. 12: Surface measurements of temperature (a), dew point(a), pressure (b), wind speed (c), and wind direction (c) at site MP1 during the bore passage. Vertical dashed line marks the estimated arrival time of the MCS outflow followed by the periodic behavior of pressure, wind, and wind speed beneath the soliton.

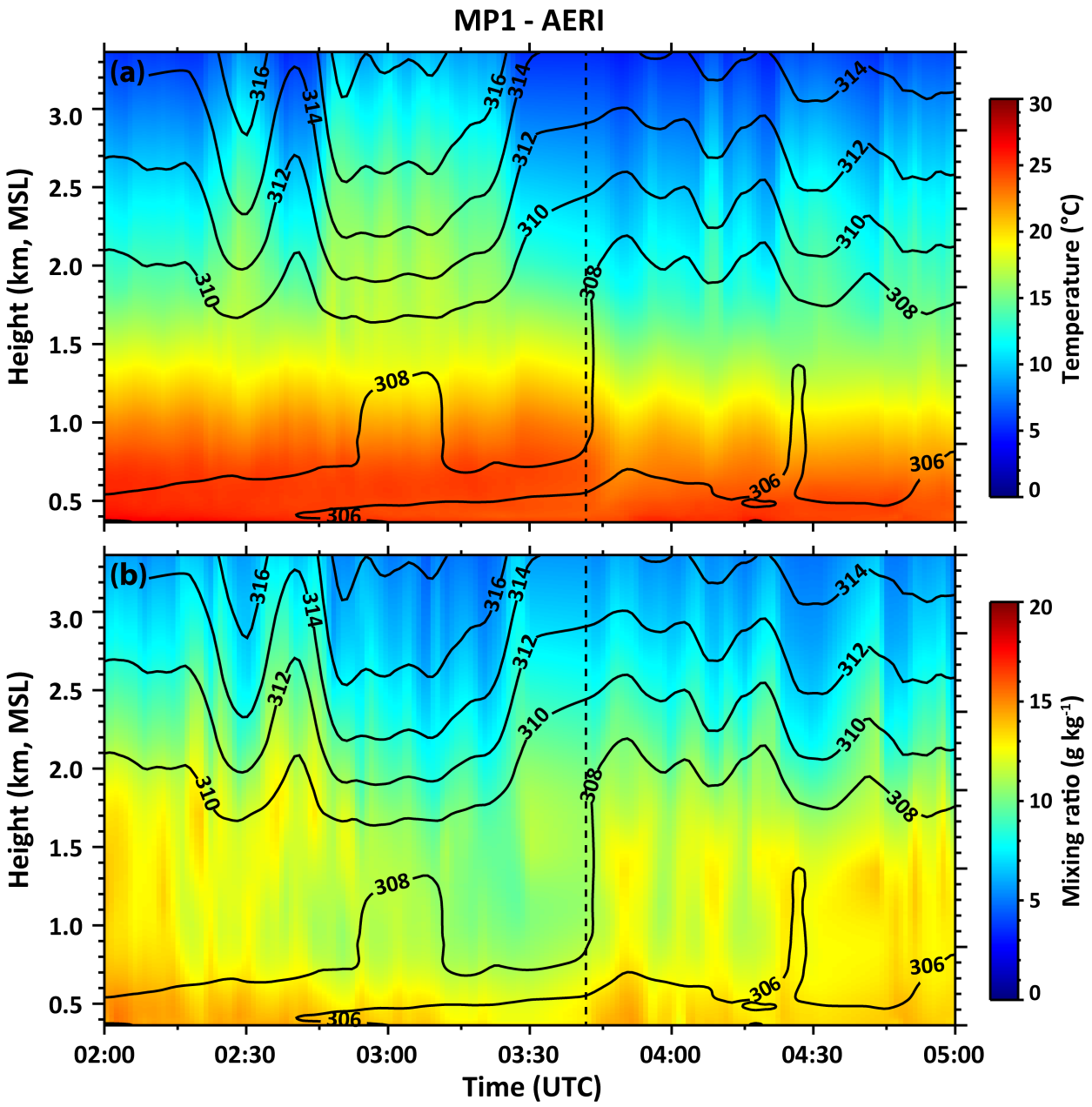

812

813 **Fig. 13.** (a) AERI temperature and (b) WVMR at MP1. Black contours are virtual potential

814 temperature. Vertical dashed line marks the estimated arrival time of the bore.

815